IVYSPRING INTERNATIONAL PUBLISHER

Theranostics

2016; 6(13): 2394-2413. doi: 10.7150/thno.16715

Review

Recent Advances in Photoacoustic Imaging for Deep-Tissue Biomedical Applications

Sheng Wang[1,2,3*], Jing Lin[1*], Tianfu Wang[1], Xiaoyuan Chen[3]✉, Peng Huang[1]✉

1. Guangdong Key Laboratory for Biomedical Measurements and Ultrasound Imaging, Department of Biomedical Engineering, School of Medicine, Shenzhen University, Shenzhen 518060, China;
2. Key Laboratory of Optoelectronic Devices and Systems of Ministry of Education and Guangdong Province, College of Optoelectronic Engineering, Shenzhen University, Shenzhen 518060, China.
3. Laboratory of Molecular Imaging and Nanomedicine, National Institute of Biomedical Imaging and Bioengineering, National Institutes of Health, Bethesda, Maryland 20892, United States.

* S.W. and J.L. contributed equally to this work.

✉ Corresponding authors: shawn.chen@nih.gov, peng.huang@szu.edu.cn.

Received: 2016.07.04; Accepted: 2016.08.16; Published: 2016.10.07

Abstract

Photoacoustic imaging (PAI), a novel imaging modality based on photoacoustic effect, shows great promise in biomedical applications. By converting pulsed laser excitation into ultrasonic emission, PAI combines the advantages of optical imaging and ultrasound imaging, which benefits rich contrast, high resolution and deep tissue penetration. In this paper, we introduced recent advances of contrast agents, applications, and signal enhancement strategies for PAI. The PA contrast agents were categorized by their components, mainly including inorganic and organic PA contrast agents. The applications of PAI were summarized as follows: deep tumor imaging, therapeutic responses monitoring, metabolic imaging, pH detection, enzyme detection, reactive oxygen species (ROS) detection, metal ions detection, and so on. The enhancement strategies of PA signals were highlighted. In the end, we elaborated on the challenges and provided perspectives of PAI for deep-tissue biomedical applications.

Key words: Photoacoustic imaging

1. Introduction

Optical imaging techniques, due to their high sensitivity, high temporal resolution and short acquisition time, have received tremendous attention in the field of biomedical applications [1-4]. However, one major challenge of optical imaging techniques is the strong light absorption/scattering of skin, tissue, blood, and so on, leading to limited tissue penetration [5-7]. Conventional optical imaging does not allow for the diagnosis of deep-seated lesions. Therefore, it is highly desirable to develop a novel optical imaging technique to overcome the above bottleneck for deep-seated tissues.

Near-infrared (NIR) optical imaging techniques (e.g. diffuse optical tomography, NIR fluorescence imaging) show great potential to overcome the limitation of tissue penetration for deep tissues imaging because NIR light (700-2,500 nm) can pass through biological tissues (e.g. skin) more efficiently than visible light [8-14]. Particularly, photoacoustic imaging (PAI), which is based on photoacoustic effect, is a promising biomedical imaging modality for deep-tissue applications [15-17]. So far, PAI has been employed to visualize hierarchical biostructures from organelles, cells to organs. As shown in Figure 1, in principle, when laser pulses are applied, some of the delivered optical energy will be absorbed by contrast agents or biological tissues and converted into heat, then a broadband ultrasonic emission will be generated due to the heat-induced transient thermoelastic expansion, which can be detected by an acoustic detector and analyzed to reconstruct PA images. PAI combines the high selectivity of optical

imaging and the deep-tissue penetration of ultrasonic imaging, so it could overcome the limitations of conventional optical imaging techniques [18].

In this paper, we will introduce recent advances of contrast agents, applications, and signal enhancement strategies for PAI. The challenges and outlooks of PAI for deep-tissue biomedical applications are also included.

2. PA contrast agents

2.1 Endogenous PA contrast agents

Some endogenous substances with special light absorption such as hemoglobin (Hb) [19], melanin [20], and lipid [21], have been used as PA contrast agents for biomedical applications (e.g. anatomical, functional and metabolic studies) [22-25]. For example, Hb is an iron-containing metalloprotein in red blood cells that carries oxygen throughout the body. According to the different light absorption spectra of oxyhemoglobin and deoxyhemoglobin, PAI is able to measure the total Hb concentration (C_{Hb}) and oxygen saturation (sO_2) [26]. Melanin, a group of natural pigments occurring in the hair, skin, and iris of the eye in most organisms, is a classical endogenous PA contrast agent with strong light absorption in both UV/vis and NIR regions [27]. Besides these agents, genetically encoded probes can also provide good PA contrast by expressing NIR-absorbing proteins, which endows PAI the ability to monitor and image gene expression [28].

2.2 Exogenous PA contrast agents

The use of exogenous PA contrast agents promises PAI with high sensitivity, specificity and signal-to-background ratio over endogenous PA contrast agents. To date, a variety of inorganic/organic PA contrast agents with strong NIR absorbance and high photothermal conversion efficiency have been explored for deep-tissue PAI. According to their structures, they are mainly categorized into inorganic and organic PA contrast agents (Table 1).

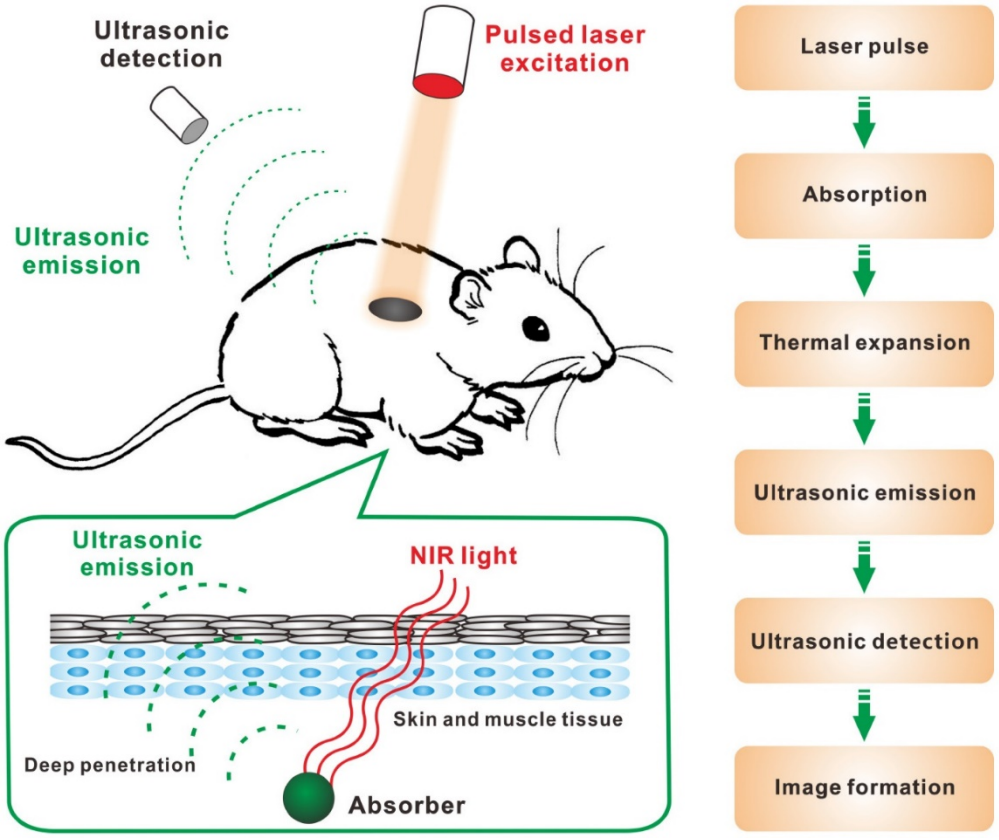

Figure 1. Schematic illustration showing the process of PAI: (1) non-ionizing laser pulses are delivered into biological tissues; (2) the delivered energy is absorbed by endogenous or exogenous contrast agents; (3) the absorbed energy is converted into heat, leading to transient thermal expansion; (4) the thermal expansion causes the generation of ultrasonic emission; (5) the generated ultrasonic emission is detected by ultrasonic transducers and (6) then analyzed for image formation.

Table 1. Examples of PA contrast agent explored in PAI.

Materials		Types of nanoagents	Advantages (+)/Disadvantages (-)	Ref.
Inorganic	Metallic nanomaterials	Au nanorods; Au nanostars; Au nanocages; Au nanoshell; Au nanovesicles; Au nanoflowers; Ag nanoplates; Palladium nanoplates; antimony nanoparticles	(+) tunable physiochemical properties; chemically inert element with reasonable biocompatibility; able to carry cargoes. (-) non-biodegradability; suboptimal photothermal stability	[29-34, 37, 38, 40-45]
	Carbon-based nanomaterials	Carbon nanotubes; Graphenes; Carbon dots	(+) able to carry cargoes; good photothermal stability. (-) non-biodegradability; heterogeneity	[47, 54, 55, 57]
	TMC	CuS; WS_2; MoS_2; FeS; Bi_2S_3; CuSe; Co_9Se_8; Bi_2Se_3	(+) high photothermal conversion efficiency; good photothermal stability; low cost. (-) non-biodegradability; contain heavy metal elements	[62-69]
Organic	Dyes	porphyrin- and cyanine-based dyes, e.g. ICG, IR780, IR825, *etc.*	(+) good biocompatibility/biodegradability. (-) poor aqueous solubility, low photothermal stability, short bloodstream circulation half-life	[77-79, 83-86]
	Polymer-based nanomaterials	Polypyrrole; Polyaniline; Polydopamine; Semiconducting polymers	(+) good biocompatibility and photothermal stability; able to carry cargoes. (-) their biodegradation behaviors remain unknown	[87-94]

2.2.1 Inorganic PA contrast agents

Metallic and semimetallic nanomaterials [29-33], especially gold nanomaterials [34], can achieve high light-to-heat conversion through localized surface plasmon resonance (LSPR), which occurs when the frequency of incident photons matches the frequency of electrons on the surface of these nanomaterials, leading to a strong optical absorption. By controlling the size/morphology of gold nanomaterials, their LSPR absorbance can be engineered into the NIR region. Moreover, gold nanomaterials have the following merits of relative inertness, prominent biocompatibility, and excellent plasmonic property. So far, various gold nanostructures (nanorods [35-38], nanostars [39, 40], nanocages [41, 42], nanoshells [43], nanovesicles [44], nanoflowers [45, 46]) with LSPR peaks in the NIR region have been explored as contrast agents for PAI as well as theranostics. However, some gold nanomaterials with suboptimal photothermal stability could be melted under pulsed laser irradiation and thus lose their NIR absorbance.

Carbon-based nanomaterials, such as carbon nanotubes [47, 48], graphenes [49-55], carbon dots [56, 57], have been widely used in biomedical applications. Carbon nanomaterials usually show broad absorbance from UV to NIR regions. In addition, a large amount of compounds/materials are easy to integrate with carbon-based nanomaterials for PAI and other functions [58-61]. However, one disadvantage of carbon-based nanomaterials is their heterogeneity. For example, carbon nanotubes are a mixture of nanotubes with different lengths and diameters.

Transition metal chalcogenides (TMC)-based nanomaterials, such as copper sulfide (CuS), tungsten sulfide (WS_2), molybdenum sulfide (MoS_2) and so on, due to energy band transitions, are a class of semiconductor nanocrystals with strong NIR absorption [62-69]. Among them, CuS nanoparticles, due to their good photothermal effect and low cost, have been extensively studied for PAI [70-73]. Despite the high photothermal conversion efficiency and good photothermal stability, TMC-based nanomaterials usually contain heavy metal elements, which limits their potential for clinical translation.

Although a lot of inorganic PA contrast agents exhibited excellent PAI performance in animal experiments, the intrinsic non-biodegradability of these agents may lead to relative long retention time and potential long-term toxicity, which limits their clinical translation [74]. Recently, black phosphorus (BP) nanomaterials with broad absorption in both UV and NIR regions, due to its excellent biodegradable property, has been used in PAI [75]. Compared with other inorganic PA contrast agents, BP nanomaterials are composed of element phosphorus without any heavy metals. Furthermore, BP nanomaterials can be fully degraded into biocompatible ions, which can be absorbed, metabolized, and cleared by the body [76].

2.2.2 Organic PA contrast agents

Besides inorganic PA contrast agents, various NIR-absorbing organic agents including porphyrin- and cyanine-based dyes, perylene-diimide (PDI) derivatives and semiconducting polymers, due to their good biodegradability and biocompatibility, have been widely developed for PAI [77-79].

In the past decades, a plethora of small molecule organic dyes have been synthesized for bioimaging [80-82]. Compared with inorganic nanomaterials, these dyes show good biocompatibility and biodegradability. Among them, indocyanine green (ICG), has been approved by the US Food and Drug Administration (FDA) and used in the clinic for a long time [83]. However, most of organic dyes suffer from poor aqueous solubility, poor photothermal stability and short bloodstream circulation half-life. To address these issues, many nanocarriers including micelles, liposomes and proteins, have been employed as the

vehicles for delivering organic dyes [79, 84-86].

A series of conducting and semiconducting polymers with conjugated structures, such as polypyrrole, polyaniline, polydopamine and so on, have also been developed as PA contrast agents [87-91]. Compared with small molecule organic dyes, polymer-based PA contrast agents showed much better photothermal stability. During the synthesis process of these polymers, many functional moieties, such as drugs (doxorubicin, sorafenib), photosensitizers (chlorin e6), contrast agents (^{64}Cu, Fe_3O_4, gadolinium, tantalum oxide), and so on, can be integrated for PAI with other imaging modalities and therapeutics [91-97]. Many *in vitro* and *in vivo* studies have demonstrated biocompatibility of these polymer-based nanomaterials [98, 99], but till now their biodegradation behaviors are still not studied in details.

3. Biomedical applications of PAI

Owing to the merits of rich contrast, high resolution and deep penetration depth, PAI has received tremendous attention as a promising noninvasive and nonionizing technique which enables multiscale and multicontrast visualization in a wide range of biomedical applications. In this section, we will summarize the biomedical applications of PAI.

3.1 Deep tumor imaging and therapy monitoring

Recently, a phosphorus phthalocyanine dye with intense absorption at 1000 nm was employed as PA contrast agent for deep PAI beyond 10 cm of chicken breast phantom and through a 5 cm human arm [100]. These results suggested that NIR light-induced PAI is a promising technique for deep-tissue diagnosis. For tumor imaging, the PA contrast agents should be tumor specific either through passive targeting or active targeting. The leaky tumor vasculature combined with poor lymphatic drainage of tumors may allow nano-sized PA contrast agents (< 100 nm) to effectively accumulate in the tumor tissue in a passive targeting manner through the so-called enhanced permeability and retention (EPR) effect [101]. In addition, with the conjugation of targeting ligands (e.g. antibodies, peptides, aptamers), PA contrast agents can actively bind to overexpressed receptors on the tumor cell membranes [102]. In a recent study, Cheng *et al*. developed perylene-diimide (PDI)-based nanoparticles as highly efficient PA contrast agents for *in vivo* deep brain tumor imaging [18]. As shown in Figure 2A, PDI molecules were encapsulated into the micelles composed of amphiphilic DSPE-mPEG. The resulting PDI-based nanoparticles with an average particle size of 48 nm were then used for detection of deep orthotopic brain tumor with high PA contrast and sensitivity (Figure 2B). Furthermore, by constructing the 3D PA image, the spatial distribution of PDI-based nanoparticles in tumor was clearly mapped. As shown in Figure 2C, the PDI-based nanoparticles were localized around the injection position of tumor cells.

Besides tumor imaging, PAI also can be used to evaluate the therapeutic efficacy of chemotherapy, photodynamic therapy, radiation therapy and antiangiogenic therapy [103-106]. For example, Hasan *et al*. used PAI to monitor the progress of photodynamic therapy (PDT) [104]. PDT is a clinical technique which exploits photosensitizers and light excitation. Upon laser irradiation, photosensitizers consume oxygen to generate cytotoxic reactive oxygen species (ROS), thus causing changes in $_SO_2$ [107]. By measuring the level of oxyhemoglobin and deoxyhemoglobin with PAI, the $_SO_2$ can be monitored and used as a marker for predicting PDT treatment efficacy. On PDT treatment, the drug-light-interval (DLI, defined as the interval between photosensitizer administration and light irradiation) plays an important role. The previous studies demonstrated that PDT with 1 h DLI was more effective when compared to PDT with 3 h DLI [108]. As shown in Figure 3, in the 1 h DLI group, clear hypoxic areas can be observed at both 6 and 24 h post-PDT; while no statistical change in $_SO_2$ value in the 3 h DLI group. These results demonstrated that PAI can be used to monitor the response to PDT by measuring $_SO_2$ change.

3.2 Metabolic imaging

PAI is also suitable for anatomical, functional and metabolic imaging, by measuring the contents of hemoglobin concentration (C_{Hb}), oxygen partial pressure (pO_2) and oxygen saturation (sO_2) [19, 22, 23]. For example, as shown in Figure 4A, the PA image of C_{Hb} reveals the vascular anatomy down to single capillaries in a living mouse ear [19]. The *in vivo* real-time oxygen unloading process can also be monitored by measuring the sO_2. As shown in Figure 4B, the sO_2 map of a capillary loop in a human finger cuticle indicated that most oxygen is unloaded from hemoglobin at the tip of the loop [24]. Based on the measurements of vessel diameter, total C_{Hb}, sO_2 and blood flow velocity, the metabolic rate of oxygen can be computed, which is helpful to understand metabolism-related pathogenic mechanisms (Figure 4C) [25]. With the help of a NIR dye-labeled 2-deoxyglucose (IRDye800-2DG), PAI can be used for *in vivo* tumor glucose metabolism imaging [109]. As shown in the PA images of orthotopically implanted

786-O kidney tumors (Figure 4D), the tumor-bearing kidney of mice displayed higher IRDye800-2DG uptake than the health kidney. At the most metabolically active site in the tumor, the tumor-to-normal kidney contrast for IRDye800-2DG uptake was approximately 3.3.

3.3 Imaging tumor microenvironment

As we know, the pH change, enzyme activity, reactive oxygen species (ROS) level, and metal ion concentration, play very important roles in life science. Aberrant behaviors of these parameters are associated with many diseases including cancer, inflammation, cardiovascular diseases, Alzheimer's disease, Wilson disease, and so on [110-113]. In the past decades, many fluorescent probes have been developed for *in vivo* detections [114-118]. Encouraged by the absorption changes of some PA contrast agents at different conditions, PAI show great potential to monitor or track the environment changes based on the readout intensity of PA signals [119-126]. Compared to traditional detection methods (e.g. fluorescence imaging), PAI promises *in vivo* quantitative detection with deep tissue penetration.

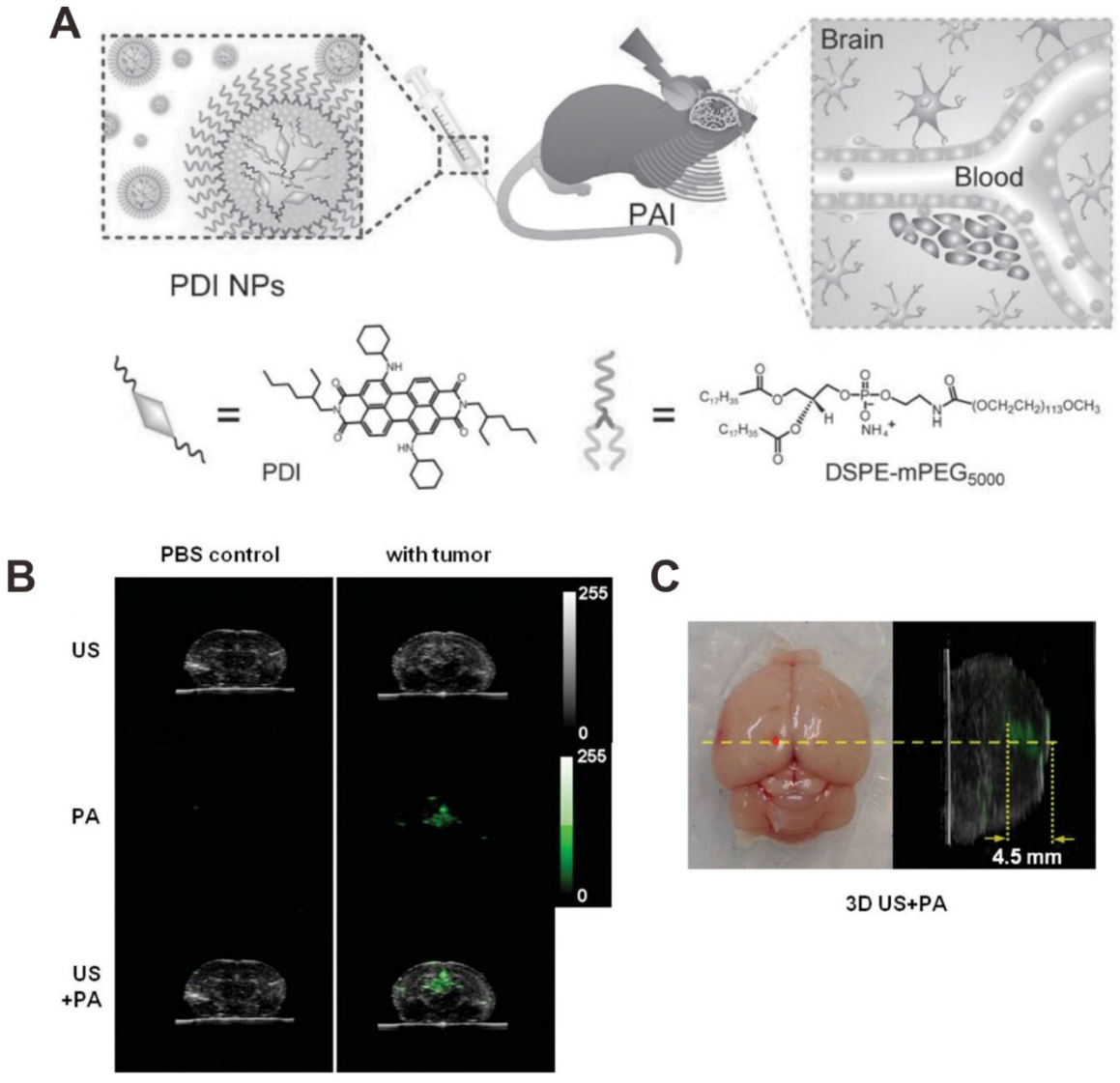

Figure 2. (A) Schematic illustration showing the structure of perylene-diimide (PDI) nanoparticles and the *in vivo* PAI process of brain tumor. (B) The ultrasonic (US), PA and their overlay images of brain coronal sections at 2 d postinjection of PDI nanoparticles. (C) Photographic transverse image (left) and PA sagittal 3D image (right) of tumor-bearing brain. The red dot is the injection point of cells. Reproduced with permission [18]. Copyright 2015 Wiley-VCH.

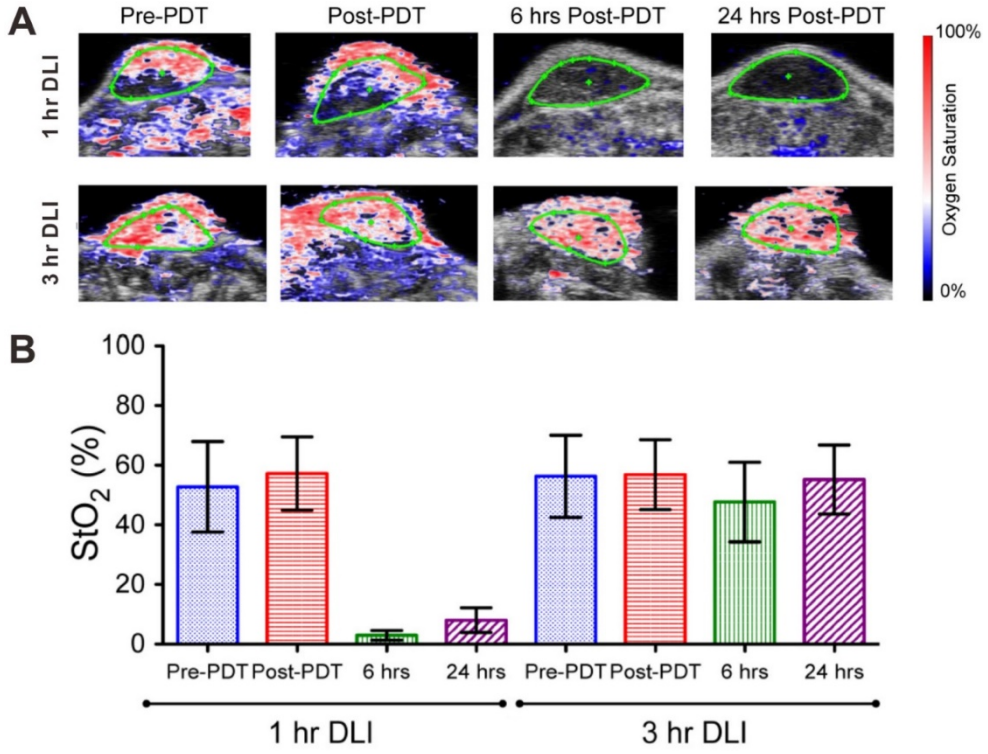

Figure 3. (A) PA images of blood oxygen saturation (StO_2) in 1 h drug-light-interval (DLI) group (up) and 3 h DLI group (down) at various time points (pre-PDT, post-PDT, 6 h and 24 h post-PDT). Blue and red signals represent hypoxic and oxygenated regions, respectively. (B) Mean StO_2 values in 1 h DLI group and 3 h DLI group. Error bars indicate standard deviation. Reproduced with permission [104]. Copyright 2015 Ivyspring International Publisher.

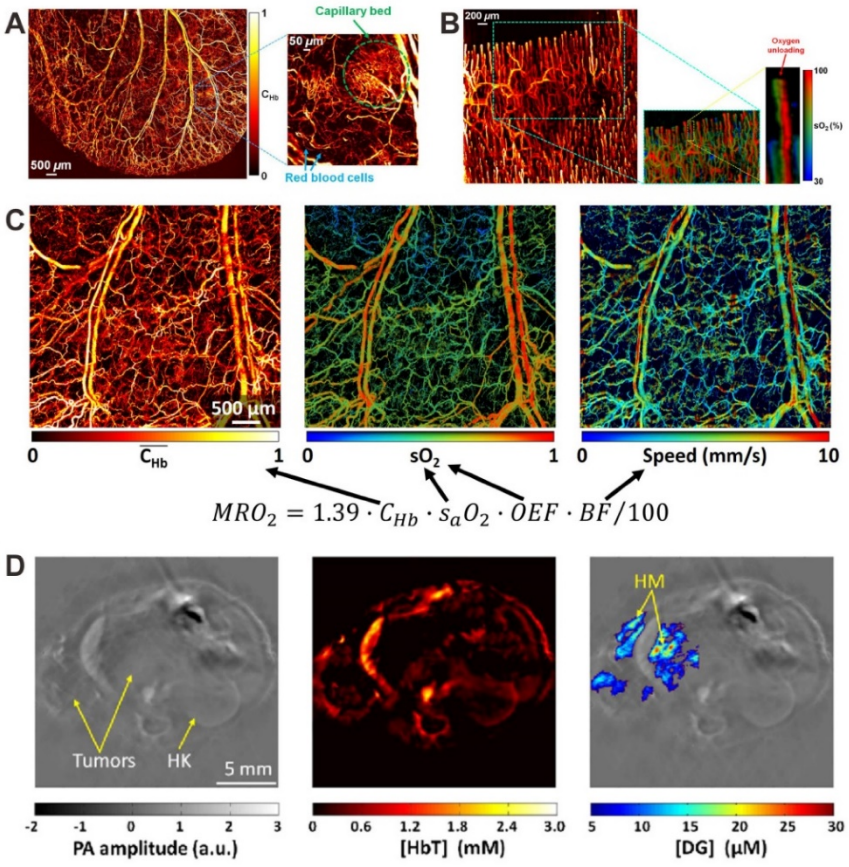

Figure 4. (A) *In vivo* PA image of relative C_{Hb} in a living mouse ear, revealing the vascular anatomy. Reproduced with permission [19]. Copyright 2011 Optical Society of America. (B) *In vivo* PA images of C_{Hb} and sO_2 in human finger cuticle. Reproduced with permission [24]. Copyright 2013 Biophysical Society. (C) *In vivo* PA images of C_{Hb}, sO_2, and blood flow speed in a nude mouse ear. Reproduced with permission [25]. Copyright 2015 Optical Society of America. (D) *In vivo* PA images of orthotopically implanted 786-O kidney tumors. Left: anatomical image; middle: total hemoglobin concentration (HbT) image; right: IRDye800-2DG concentration (DG) image; HK: healthy kidney; HM: hypermetabolic. Reproduced with permission [109]. Copyright 2012 SPIE

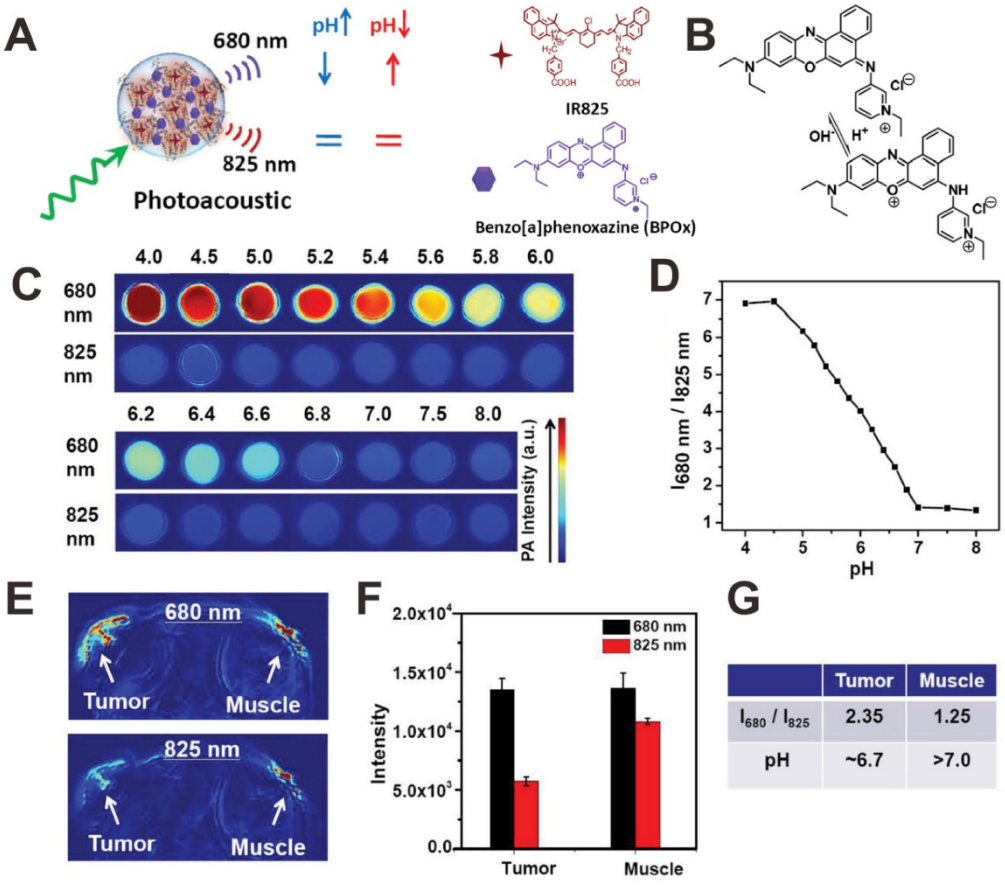

Figure 5. (A) Illustration showing the mechanism of albumin-BPOx-IR825 complex for pH detection. (B) The structure change of BPOx under different pHs. PA images (C) and signal intensity ratios (D) in response to various pH values. PA images (E) and PA signals (F) of a mouse with local administration of HSA-BPOx-IR825 in its tumor (left side) or muscle (right side). (G) The quantitative analysis of pH value in the tumor and muscle. Reproduced with permission [119]. Copyright 2015 Wiley-VCH.

3.3.1 pH detection

Since many diseases such as cancer are always accompanied by pH change at the microenvironment [110], the *in vivo* real-time pH detection may be a potential indicator for early recognition, diagnosis, monitoring, and prognosis of diseases. In order to detect pH *in vivo*, recently, some organic dyes with pH-responsive NIR absorption shift have been exploited as PA contrast agents for PA pH detection [119-121]. For example, Liu *et al.* developed a pH-responsive nanoprobe based on albumin-benzo[*a*]phenoxazine (BPOx)-IR825 complexes (HSA-BPOx-IR825) for *in vivo* ratiometric PA pH imaging (Figure 5A) [119]. Along with the decrease of pH, the IR825 absorbance peak at 825 nm showed no obvious change; however, the absorbance at 670-680 nm significantly increased through the protonation and intramolecular charge-transfer of BPOx (Figure 5B). Therefore, the PA signal intensity at 680 significantly increased while PA signal intensity at 825 nm showed negligible change (Figure 5C). In the pH range of 5.0-7.0, the ratiometric PA signal ($PA_{680\ nm}/PA_{825\ nm}$) showed excellent pH dependence, which is suitable for PA imaging of tumor microenvironment (Figure 5D). *In vivo* pH detection of tumor and muscle was then carried out on a mouse model *via* the local administration of HSA-BPOx-IR825. As shown in Figure 5E and F, in the tumor region, the PA intensity at 680 nm was much stronger than that at 825 nm, resulting in relatively high PA signal ratio ($PA_{680\ nm}/PA_{825\ nm}$ = 2.35). In contrast, the PA signal ratio in the muscle region ($PA_{680\ nm}/PA_{825\ nm}$ = 1.25) was obviously lower than that in the tumor. As shown in Figure 5G, the pH values of tumor and muscle were determined to be ≈6.7 and >7.0 based on the standard calibration curve in Figure 5D, which demonstrated that the HSA-BPOx-IR825 could be used as a PA contrast agent for pH detection *in vivo*. In another study, as shown in Figure 6A, Pu *et al.* developed an activatable PA nanoprobe (SON), which consists of a semiconducting oligomer (SO, inert PA matrix) and a boron-dipyrromethene dye (pH-BDP, pH indicator) [122]. Under tumor acidic environment, the hydroxyl group of pH-BDP can undergo protonation, thus leading to the absorption changes of SON. With the pH decrease, the absorption peak at 750 nm decreased significantly, while the absorption peak at 680 nm remained unchanged (Figure 6B). Consequently, the

PA intensity at 750 nm also dropped along with the decrease of pH (Figure 6C and D). Therefore, the ratiometric PA signals ($PA_{680\ nm}/PA_{750\ nm}$) were used to quantify pH (Figure 6E). For *in vivo* pH detection, SON was locally injected into tumor and muscle in living nude mice. Then PA images were recorded under the excitation of 680 and 750 nm lasers, respectively. As shown in Figure 6F, relatively high PA signals at both 680 and 750 nm were detected in the muscle; while in the tumor site, the PA intensity at 750 nm was obviously lower than that at 680 nm. To minimize the interference of endogenous PA contrast agents (e.g. hemoglobin), the PA intensity increments (PA intensity after injection of samples subtracted by the tissue background intensity before injection) at 680 and 750 nm ($\Delta PA_{680\ nm}$ and $\Delta PA_{750\ nm}$) were used to evaluate the *in vivo* pH. Quantification of the ratiometric PA intensity increments ($\Delta PA_{680\ nm}/\Delta PA_{750\ nm}$) showed that the $\Delta PA_{680\ nm}/\Delta PA_{750\ nm}$ in the tumor was higher than that in the muscle, suggesting a lower pH value in the tumor region (Figure 6G).

3.3.2 Enzyme detection

Matrix metalloproteinases (MMPs), a family of zinc-dependent endopeptides that degrade proteins in the extracellular matrix, not only take action in tumor angiogenesis, but also are involved in multiple signaling pathways [127]. To detect MMPs *in vivo*, Liu *et al.* conjugated NIR-absorbing CuS nanoparticles with a black hole quencher 3 (BHQ3) *via* a MMP-cleavable peptide linker (Figure 7A) [124]. As shown in Figure 7B, the as-prepared CuS-peptide-BHQ3 (CPQ) showed PA signals at 680

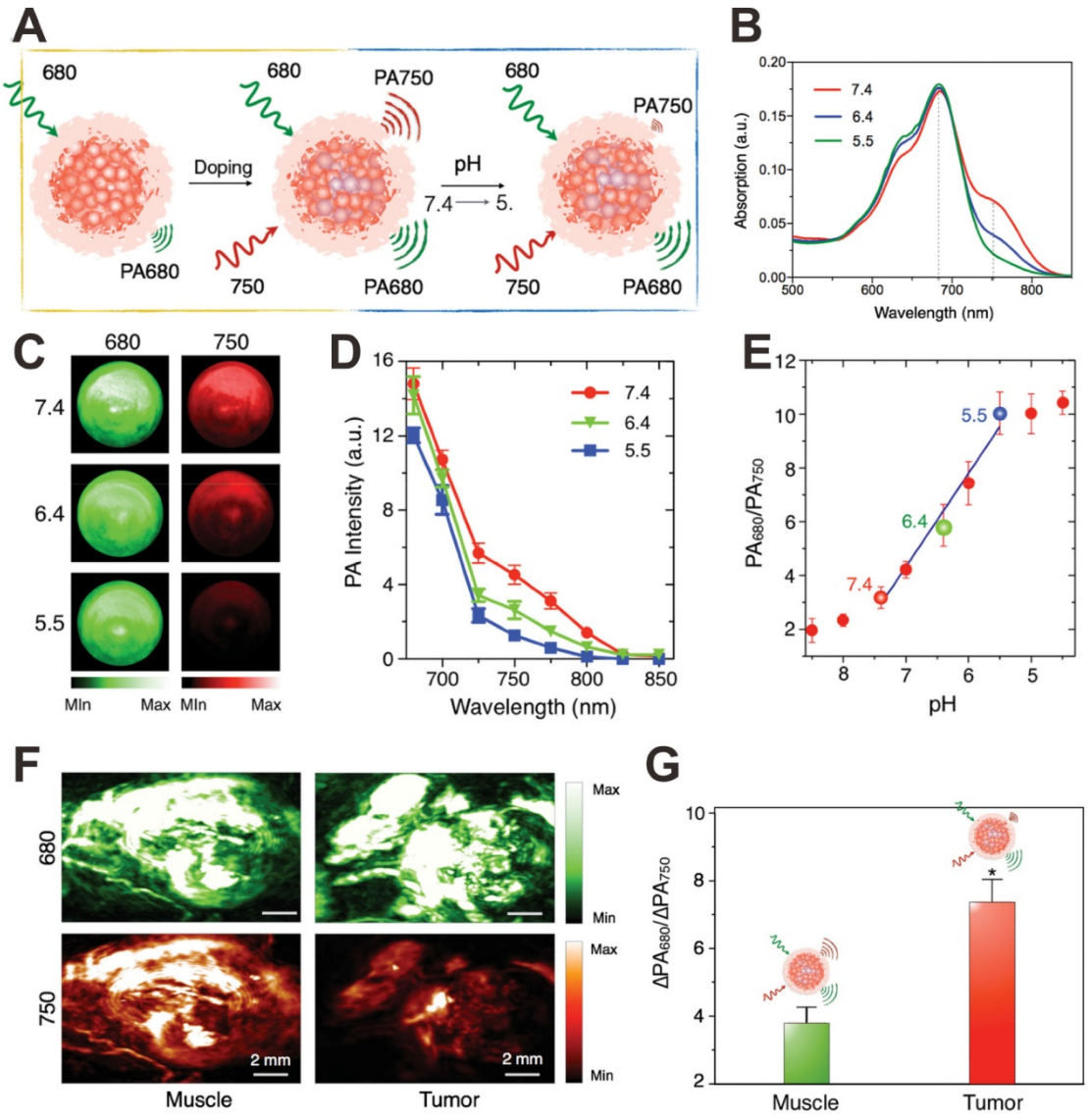

Figure 6. (A) Illustration showing the mechanism of activatable PA nanoprobe (SON) for pH detection. Absorption spectra (B), PA images (C), PA spectra (D) and ratiometric PA signals (680/750) (E) of SON at different pH. *In vivo* PA images (F) and ratiometric signals (G) of muscle and tumor with local injection of SON. Reproduced with permission [122]. Copyright 2016 Wiley-VCH.

nm (owing to BHQ3 absorbance) and 930 nm (owing to CuS absorbance). In the presence of MMPs, the BHQ3 would be released from the CuS nanoparticles due to the cleavage of peptide linker, leading to the decrease of absorption peak at 630 nm (Figure 7C). In the tumor microenvironment, the small molecule BHQ3 would be rapidly metabolized after cleavage, while the CuS nanoparticles would be retained in the tumor. The ratiometric PA signals ($PA_{680\ nm}/PA_{930\ nm}$) were used as an *in vivo* indicator of MMPs activity (Figure 7D). Xing *et al.* developed a MMP_2 antibody conjugated gold nanorod (AuNR-Abs), which can specifically target MMP_2 to achieve PAI detection of MMP_2 in atherosclerotic plaques [123]. The results demonstrated the feasibility of quantitative PA detection of MMP_2 in atherosclerotic plaques.

3.3.3 ROS detection

Recently, Rao *et al.* reported an *in vivo* real-time PA ROS detection method [125]. As shown in Figure 8A, IR775S, a cyanine dye that can sense specific ROS-mediated oxidation [128], was loaded into a semiconducting polymer nanoparticle (SPN) composed of poly(cyclopentadithiophene-*alt*-benzothiadiazole) (SP1). The PA spectrum of obtained ratiometric photoacoustic probe (RSPN) showed three PA peaks at 700, 735 and 820 nm, respectively. In the presence of $ONOO^-$ and ClO^-, the PA peak of IR775S at 820 nm decreased significantly due to the ROS-mediated decomposition of IR775S (Figure 8B); while the peak of SP1 at 700 nm had negligible change (Figure 8C). Thus the ROS level can be evaluated according to the change of ratiometric PA signals ($PA_{700\ nm}/PA_{820\ nm}$) (Figure 8D). In order to build an *in vivo* model, zymosan, a structural polysaccharide that can simulate the generation of ROS, was injected intramuscularly into the thigh of living mice. After 20 min, RSPN was injected into the same location and the PA signals at both 700 nm and 820 nm were monitored simultaneously. As shown in Figure 8E, for the mice without zymosan treatment, the PA signals at both 700 nm and 820 nm remained nearly unchanged over time. In contrast, the PA signal at 820 nm for the mice with zymosan treatment significantly decreased over time, resulting in an increased $PA_{700\ nm}/PA_{820\ nm}$ value (Figure 8F). Thus, RSPN can be used as a PA probe for *in vivo* effective detection of ROS.

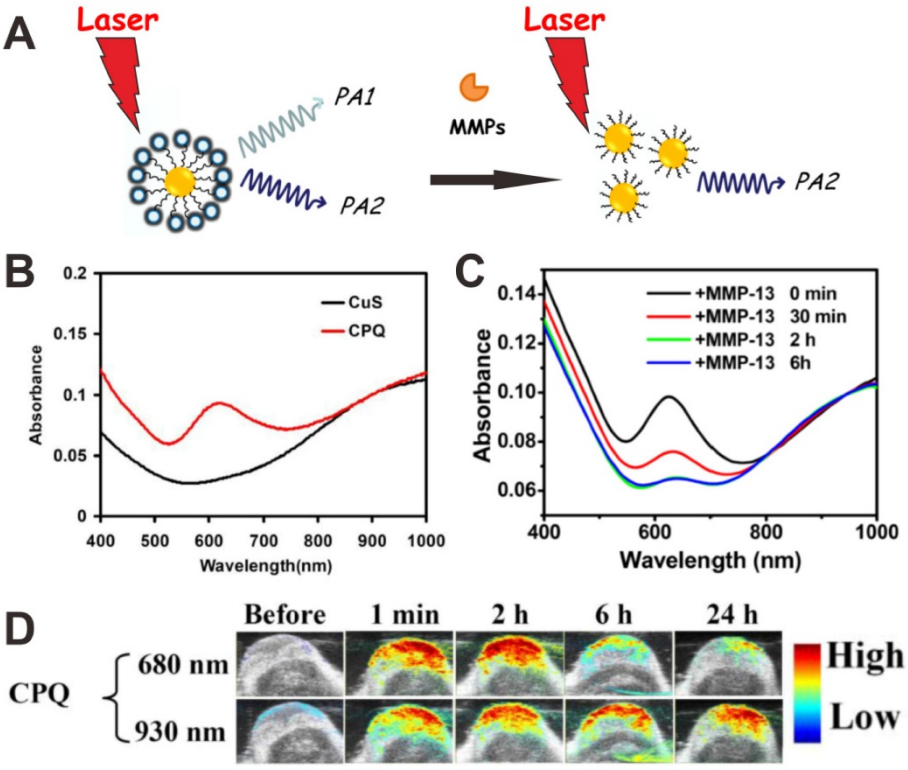

Figure 7. (A) Mechanism of CuS-peptide-BHQ3 (CPQ) for MMP detection by using PAI. (B) Absorption spectra of CuS nanoparticles and CPQ. (C) Time-dependent absorbance spectra of CPQ incubated with matrix metalloproteinase-13 (MMP-13). (D) *In vivo* PA images showing CPQ response to MMP-13. Reproduced with permission [124]. Copyright 2014 Ivyspring International Publisher.

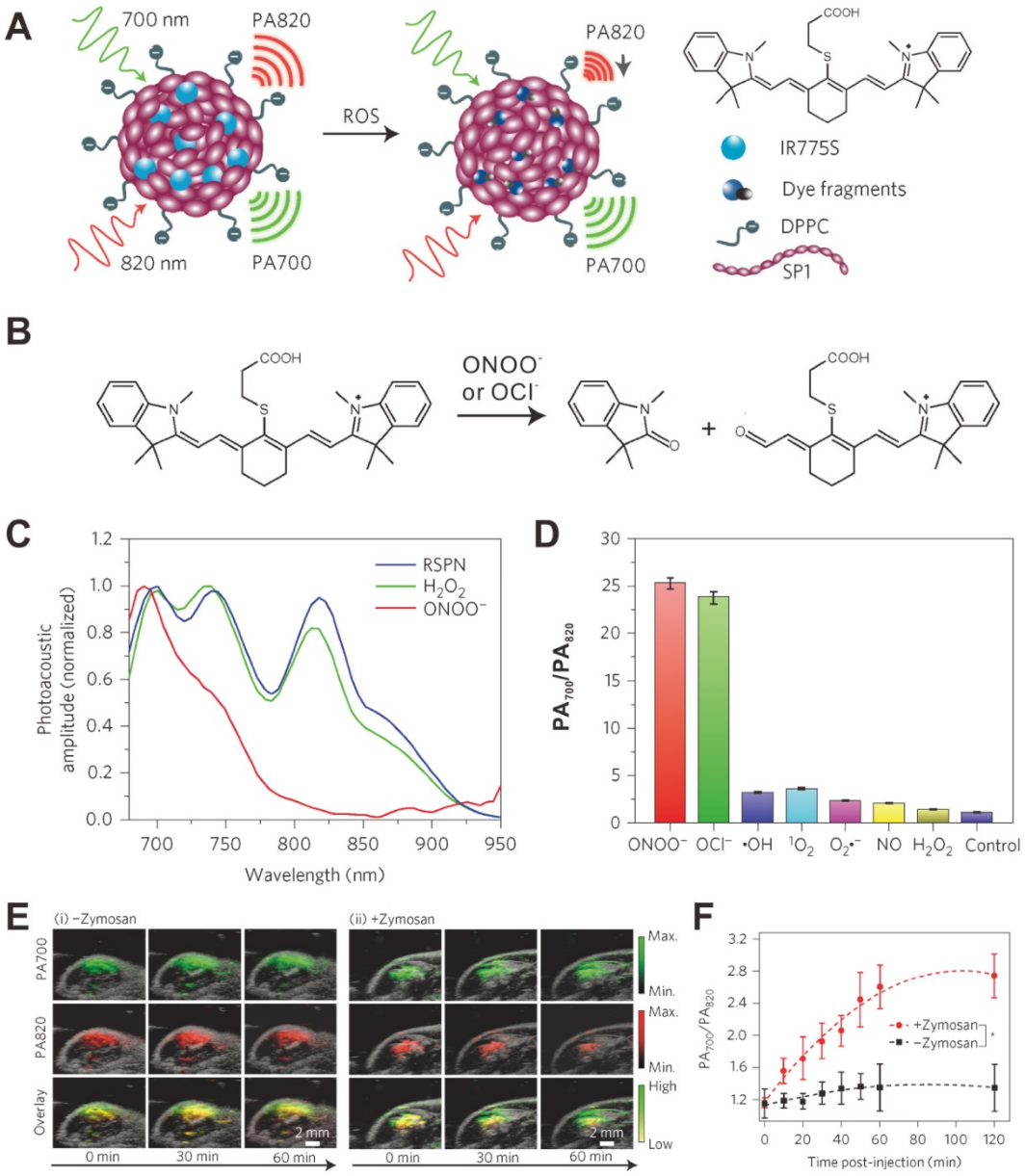

Figure 8. (A) Mechanism of ratiometric photoacoustic probe (RSPN) for reactive oxygen species (ROS) detection. (B) The structure change of IR775S in response to ROS. (C) PA spectra of RSPN in the absence and presence of ROS. (D) Ratio of PA amplitude (PA_{700}/PA_{820}) after ROS treatment. (E) PA images of saline (i) and zymosan (ii) treated thigh regions in a murine model of acute oedema. (F) Ratiometric PA signals (700/820) as a function of time post-injection of RSPN. Reproduced with permission [125]. Copyright 2014 Nature.

3.3.4 Metal ion detection

PAI also can be used to detect metal ions, such as copper (Cu^{2+}) and lithium (Li^{+}). For example, Chan *et al.* developed a PA probe for the chemoselective visualization of Cu^{2+}, which is a crucial metal ion in chronic nervous diseases (e.g. Alzheimer's disease) [126]. As shown in Figure 9A, the acoustogenic probe for Cu^{2+}-2 (APC-2) contains a 2-picolinic ester sensing module that can specifically respond to Cu^{2+}. In the absence of Cu^{2+}, the PA signal of the probe at 767 nm will be lower than that at 697 nm, leading to a small ratiometric PA_{767} nm/PA_{697} nm. In the presence of Cu^{2+}, the sensitive module hydrolyzed, a stronger PA signal at 767 nm and a weaker PA signal at 697 nm will be detected, resulting in a large ratiometric PA_{767} nm/PA_{697} nm (Figure 9B). Based on the ratiometric PA_{767} nm/PA_{697} nm change, the Cu^{2+} can be detected (Figure 9C). Due to the high selectivity and the deep-tissue penetration of PAI, this PA probe shows great potential for *in vivo* Cu^{2+} detection. In another study, Clark *et al.* developed a PA nanosensor for *in vivo* Li^{+} detection [129]. As shown in Figure 9D, the nanosensor is mainly composed of a lithium selective crown ether ionophore, lithium ionophore VI (L), and a chromoionophore (CH^{+}). Li^{+} is recognized and extracted into the hydrophobic polymer core of the nanosensor, leading to the deprotonation of CH^{+}, which changes the optical properties of the

nanosensor. As a result, the photoacoustic amplitude at 515 nm increase and the photoacoustic amplitude at 660 nm decreases (Figure 9E). For *in vivo* detection of Li^+, the nanosensor was injected into the skin of mice and imaged with PA tomography (Figure 9F). Upon intraperitoneal administration of lithium (38 mg/kg), the ratiometric $PA_{515\ nm}/PA_{660\ nm}$ of the nanosensor increased by 25% in 14 min (Figure 9G). To date, many organic dyes that can respond to metal ions and realize absorbance change have been developed for fluorescence detection [130-132], which could be utilized for PA metal ions detection.

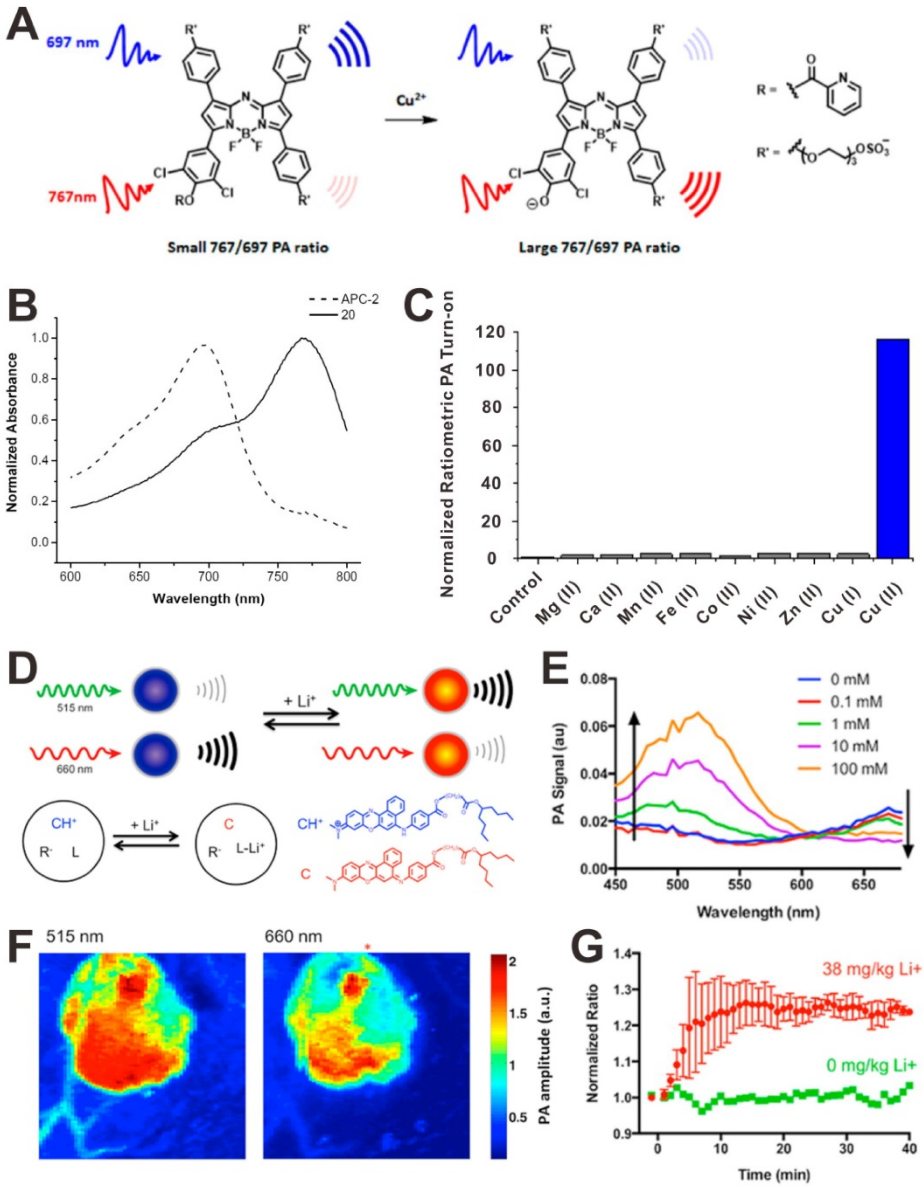

Figure 9. (A) Mechanism of PAI for Cu^{2+} detection. (B) Normalized absorbance spectra of acoustogenic probe for Cu^{2+}-2 (APC-2) and its hydrolyzed product (**20**). (C) PA signal responses of APC-2 to various metal ions. Reproduced with permission [126]. Copyright 2015 American Chemical Society. (D) The principle of PAI for Li^+ detection. (E) PA signal responses of nanosensor to Li^+. (F) *In vivo* dual wavelength PA images of mice. (G) Ratiometric PA signals (515/660) as a function of time post-injection of Li^+. Reproduced with permission [129]. Copyright 2015 American Chemical Society.

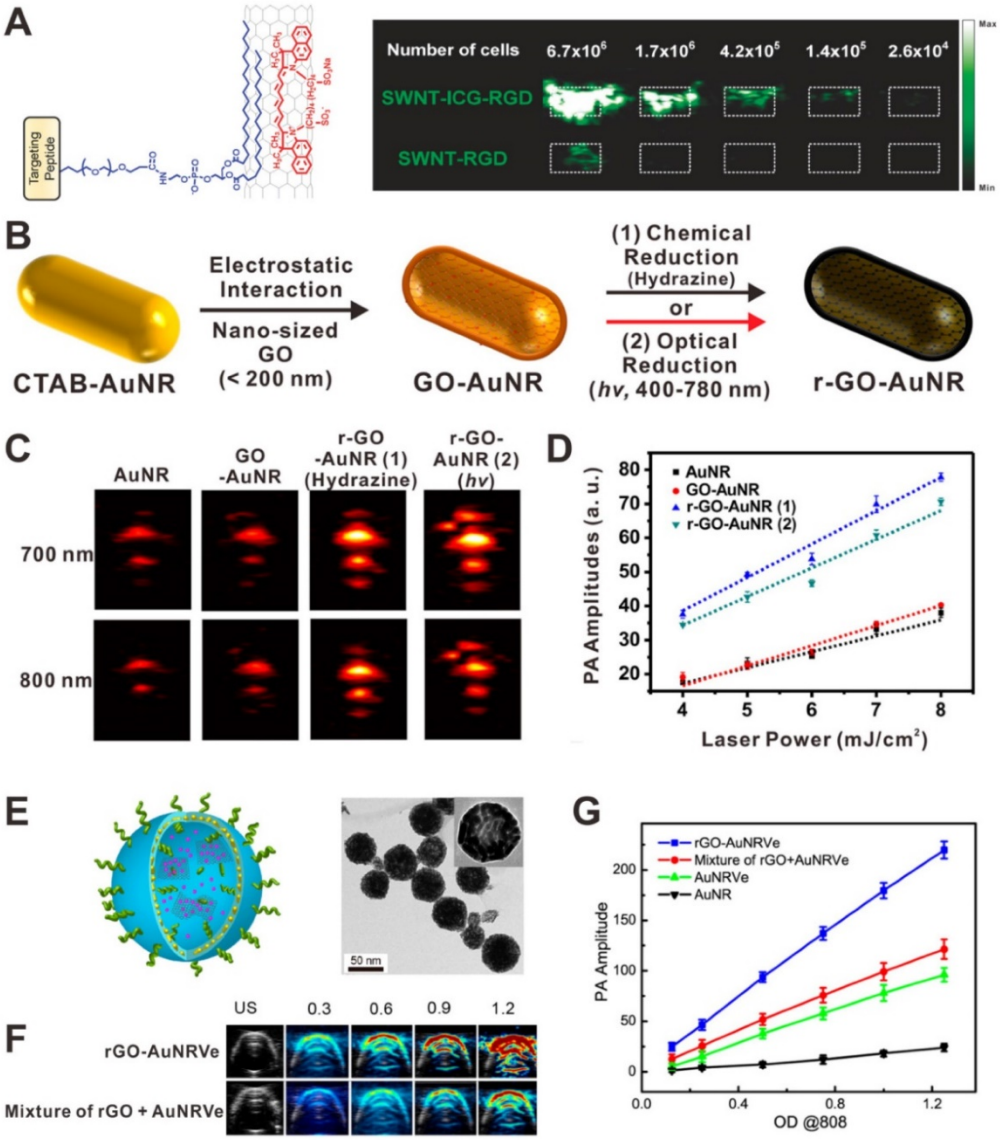

Figure 10. (A) Illustration of an indocyanine green (ICG) coated single-walled carbon nanotubes (SWNTs) and PA image of agarose phantoms containing U87MG cells exposed to SWNT-ICG-RGD and SWNT-RGD. Reproduced with permission [136]. Copyright 2010 American Chemical Society. (B) Illustration showing the synthesis process of graphene oxide (GO)-coated gold nanorods (GO-AuNRs) and reduced graphene oxide (rGO)-coated gold nanorods (rGO-AuNRs). *In vitro* PA images (C) and PA intensities (D) of AuNRs, GO-AuNRs, rGO-AuNRs (1), and rGO-AuNRs (2). Reproduced with permission [135]. Copyright 2015 American Chemical Society. (E) Illustration and TEM image of rGO-loaded gold nanorod vesicle (rGO-AuNRVe). *In vitro* PA images (F) and PA intensities (G) of samples. Reproduced with permission [137]. Copyright 2015 American Chemical Society.

4. Strategies to enhance PA signals

The PA signal enhancement strategies are critical for improving the sensitivity of both diagnosis and detection. Different strategies for PA signal enhancement, such as synergistic effect, plasmonic coupling effect, self-assembly, photoinduced electron transfer, as well as background signal deduction will be summarized in this section.

4.1 Synergistic effect

A simple way to amplify the PA signal is the combination of two or more PA contrast agents together to achieve higher absorbance. Various nanocomposites have been developed for the amplification of PA signals, such as dye-graphene [133], gold-graphene [134, 135]. The PA signal amplification mechanisms of these nanocomposites mainly include absorption superposition [136], interaction of different agents [137] and reduced heat transfer resistance [135]. For example, Gambhir *et al.* developed a family of composites based on single-walled carbon nanotubes (SWNTs) and organic dyes for highly sensitive PAI [136, 138]. As shown in Figure 10A, compared with plain SWNTs, the indocyanine green (ICG)-coated SWNTs exhibited a 20-fold higher absorbance due to the absorption superposition of both dyes and SWNTs. Thus the ICG-coated SWNTs showed higher PA contrast and can easily detect ~20 times fewer cancer cells. Lim and

co-workers reported a hybrid PA contrast agent (rGO-AuNR), composed of gold nanorods and reduced graphene oxide (rGO), for sensitive PAI [135]. GO-coated gold nanorods (GO-AuNRs) were prepared through simple electrostatic interactions. After chemical or optical reduction, rGO-AuNRs were successfully prepared (Figure 10B). In this case, rGO can not only enhance NIR light absorption *via* absorption superposition, but also reduce heat transfer resistance from the gold nanorods to the ambient signal-generating medium. The results demonstrated that the rGO-AuNRs exhibit significantly amplified PA signal intensity when compared to AuNRs and GO-AuNRs (Figure 10C and D). Chen *et al.* reported a hybrid rGO-loaded gold nanorod vesicle (rGO-AuNRVe) for sequential drug release and enhanced photothermal and PA effect (Figure 10E) [137]. Compared with the simple mixture of AuNRVe and rGO, the rGO-AuNRVe showed remarkably amplified PA signal at the same OD_{808} value (Figure 10F and G). It is believed that the cavity of gold nanorod vesicle can concentrate the electromagnetic radiations, resulting in the absorption efficiency enhancement of the encapsulated rGO [139].

4.2 Plasmonic coupling effect

Plasmonic nanostructures, such as gold nanomaterials, have been actively studied as PA contrast agents. Since the size of the nanomaterials are much smaller than the wavelength of light, the lateral and vertical finite spacing will lead to strong interaction between the neighboring elements. Compared to an individual element, the optical properties of plasmonic nanostructures will be changed substantially [140]. With the distance decrease of adjacent gold nanoparticles, the plasmonic coupling effect would be significantly enhanced, which promises the PA signal amplification. For example, Chen *et al.* developed a plasmonic biodegradable gold nanovesicle (BGV) by the self-assembly of polymer-tethered gold nanoparticles [141]. As shown in Figure 11A, in the formation process of BGV, the distance (*d*) between adjacent gold nanoparticles reduced, leading to an ultrastrong plasmonic coupling effect. Plasmonic coupling between gold nanoparticles can generates enhanced electromagnetic field, resulting in enhanced photothermal conversion efficiency and thus amplified PA signals (Figure 11B and C). In a more recent study, they further demonstrated that the chain gold vesicle, self-assembled through a stepwise hierarchical self-assembly process, had stronger plasmonic coupling effect than the non-chain vesicle, and therefore achieved PA signal amplification (Figure 11D and E) [142]. Based on the same principle, the developed plasmonic gold bellflowers (GBFs) which also amplified the PA signals because of the presence of strong plasmonic coupling effect among the multiple-branched petals (Figure 11F) [45]. The PA signal intensities of GBFs were much stronger than that of gold nanorods (GNRs) and gold nanostars (GNSs) at the same OD_{808} value (Figure 11G). This PA enhancement strategy is suitable for plasmonic metal nanomaterials, such as gold, silver, and so on.

4.3 Self-assembly

A *J*-aggregate is a type of nanoassembly when dye molecules aggregate under the influence of certain conditions. Compared to dye monomer, *J*-aggregate shows red-shifted absorption wavelength and higher absorption coefficient [143]. Therefore, the use of a self-assembly nanostructure is another strategy to amplify the PA signals of organic dyes [144-146]. For example, Chen *et al.* reported an *in situ* tumor-specific supramolecular self-assembly (ICG doped nanofiber) for enhanced PAI [147]. The mixture of ICG and an alkaline phosphatase (ALP)-responsive peptide forms micelles, which can efficiently self-assemble into nanofibers in the ALP-rich tumor macroenvironment (Figure 12A). As shown in Figure 12C and D, the PA signal of nanofibers in tumor site was much stronger than that of ICG. This excellent performance of nanofibers in PAI was mainly attributed to their unique *in situ* self-assemble features: (i) the *J*-aggregate structure of ICG in nanofibers induced an amplified PA signal (Figure 12B), and (ii) the assembly induced enhanced tumor retention. Based on a similar strategy, Wang and co-workers designed an enzyme-responsive small-molecule precursor **1**, which had three functional segments: purpurin 18 (P18) as the NIR dye, enzyme-responsive peptide (PLGVRG) as the linker, and RGD peptide as the targeting ligand [144]. As shown in Figure 12E, in the presence of gelatinase, which is overexpressed in tumor, the PLGVRG linkers was cleaved, and then the residues self-assembled into nanofibers due to the enhanced hydrophobicity and reduced steric hindrance. Compared to **2** (P18-PMGMRGRGD without responsiveness) and **3** (P18-PLGVRGRDG without targeting), **1** showed a significantly amplified PA signal, which was attributed to the assembly induced signal amplification and assembly induced retention effect (Figure 12F). This similar strategy was also used for bacterial infection detection [145]. This self-assembly PA enhancement strategy is suitable for organic dyes by forming ordered arrangement, such as *J*-aggregates.

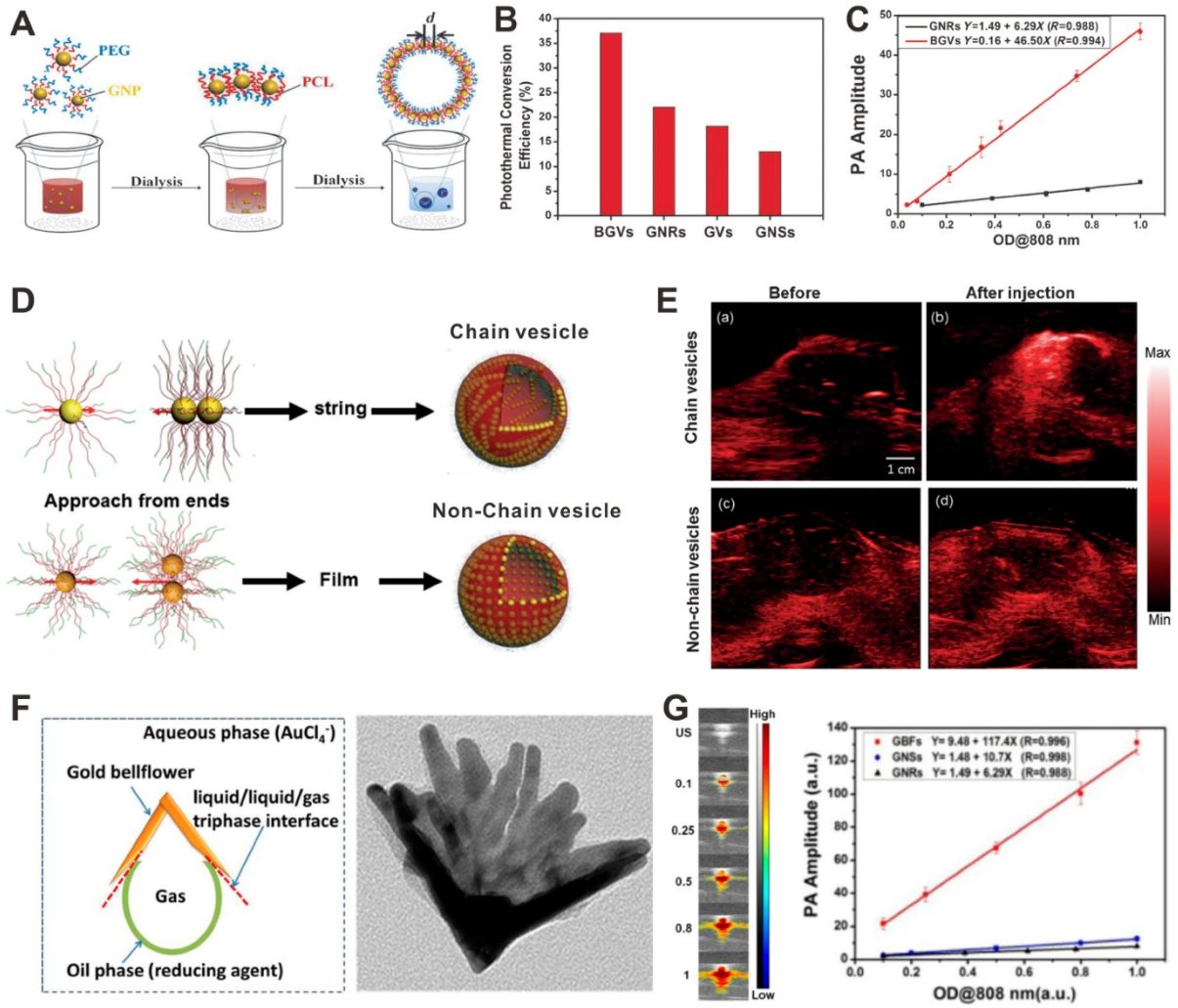

Figure 11. (A) Illustration showing the formation process of biodegradable gold nanovesicles (BGVs). (B) Photothermal conversion efficiencies of BGVs, gold nanovesicles (GVs), gold nanorods (GNRs) and gold nanostars (GNSs). (C) PA signals of BGVs and GNRs as a function of OD_{808} values. Reproduced with permission [141]. Copyright 2013 Wiley-VCH. (D) Illustration showing the formation of chain and non-chain vesicles. (E) PA images of mouse tissues before and after the injection of chain vesicles (a, b) or non-chain vesicles (c, d). Reproduced with permission [142]. Copyright 2015 Wiley-VCH. (F) The formation process and TEM image of gold bellflowers (GBFs). (G) PA images and signals of GBFs at different OD_{808} values. Reproduced with permission [45]. Copyright 2014 American Chemical Society.

4.4 Photoinduced electron transfer (PET)

PET is a transfer process of excited state electron, in which excited electron is transferred from donor to acceptor. This strategy is able to enhance the nonradiative heat generation, which can be used for PA signal amplification [148]. Pu *et al.* developed a fullerene doped semiconducting polymer nanoparticle (SPN-F) that can amplify the PA signal through the intraparticle photoinduced electron transfer [148]. As shown in Figure 13A, the lowest unoccupied molecular orbital (LUMO) and highest occupied molecular orbital (HOMO) are -3.5 and -4.9 eV for semiconducting polymer and -4.3 and -6.5 eV for fullerene, respectively. Therefore, the semiconducting polymer and fullerene play their roles as electron donor and acceptor, respectively, leading to quenched fluorescence and enhanced nonradiative heat generation upon light irradiation, ultimately achieve amplified PAI signal. As shown in Figure 13B and C, with increasing amount of fullerene doped (SPN-Fx, x: the weight percentages of fullerene), the PA intensity obviously increased. The amplified PA signals of SPNs have also been demonstrated *in vivo*. As shown in Figure 13D and E, compared to SPN-F0 injected mice, the mice injected with SPN-F20 exhibited much higher PA signals in the tumor at all the time points.

4.5 Background signal deduction

Besides the above mentioned strategies for PA signal amplification, the strategy of PA background signal deduction is another way to indirectly enhance the PA signal. For example, Wang *et al.* reported a reversibly switchable bacterial phytochrome based PA probe for *in vivo* tumor detection with substantially decreased background signals [149]. As shown in Figure 14A, upon light illumination,

rhodopseudomonas palustris (BphP1) can be reversibly switched between Pfr (ON-state) and Pr (OFF-state). Because the PA background signal of vascular absorbers remains relatively constant, this switchable property of PA probe allows to subtract the two obtained PA images under individual states, and completely remove the background signals (Figure 14B and C), thus achieving enhanced detection sensitivity and improved spatial resolution (Figure 14D). In another study, Gao *et al.* reported iron oxide and gold-coupled core-shell nanoparticles (MNP-Au) for magnetomotive PAI (mmPAI) [150]. As shown in Figure 14E, a pulsed magnetic field is applied during PA signal acquisition. MNP-Au particles move and create a moving source when the field is on, and then return to their original positions when the field is off. In contrast, the non-magnetic background PA sources do not move during this process. Therefore, coherent motion processing of a PA image sequence can identify sources related to MNP-Au and reject all diffuse and localized background signals. Then both conventional PAI and mmPAI were performed using gold nanorod (Au NR) to mimic strong background tissue signals. As shown in Figure 14F, compared to conventional PAI, the Au NR mimicking a strong background signal is almost completely suppressed in mmPAI.

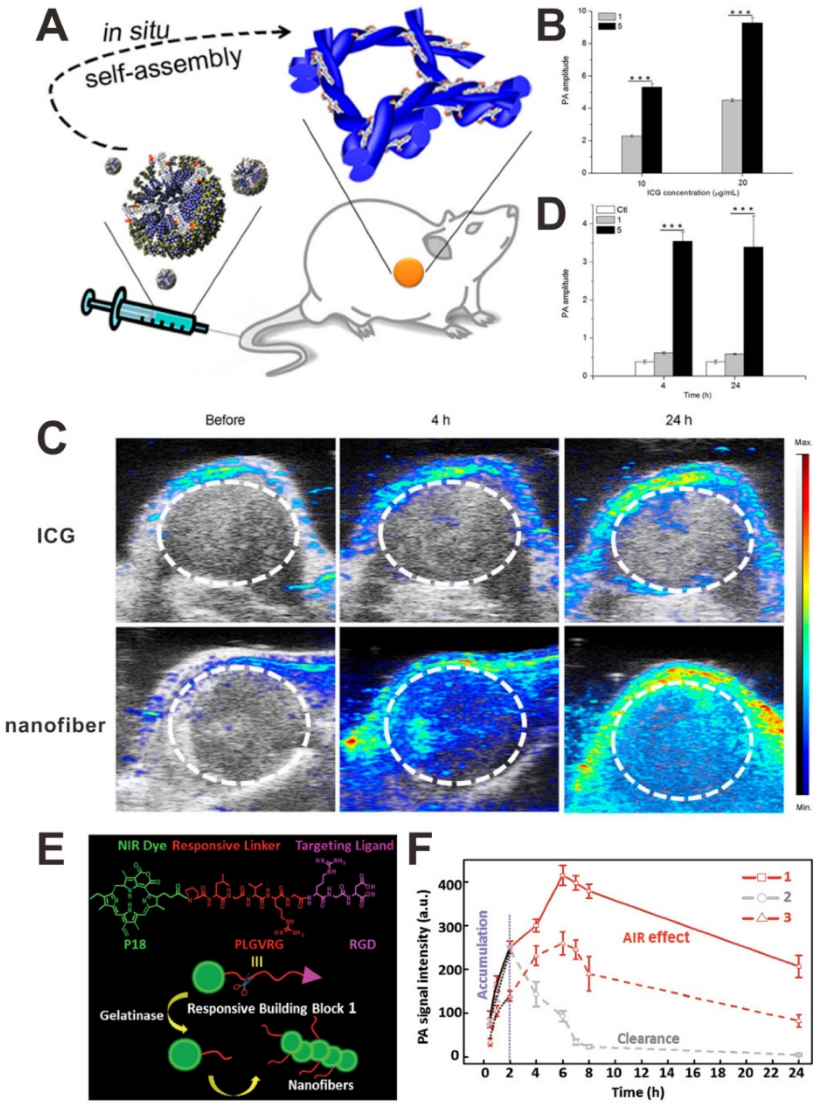

Figure 12. (A) Illustration showing the *in situ* formation of nanofibers. (B) PA intensity changes of ICG (**1**) and nanofiber (**5**) at different ICG concentrations. PA images (C) and PA intensities (D) of tumor tissues after intravenous injection of samples. Reproduced with permission [147]. Copyright 2015 American Chemical Society. (E) Illustration showing the structure of compound **1** and the *in situ* formation of nanofibers. (F) PA signal intensities of tumor sites after intravenous injection of samples. Reproduced with permission [144]. Copyright 2015 Wiley-VCH.

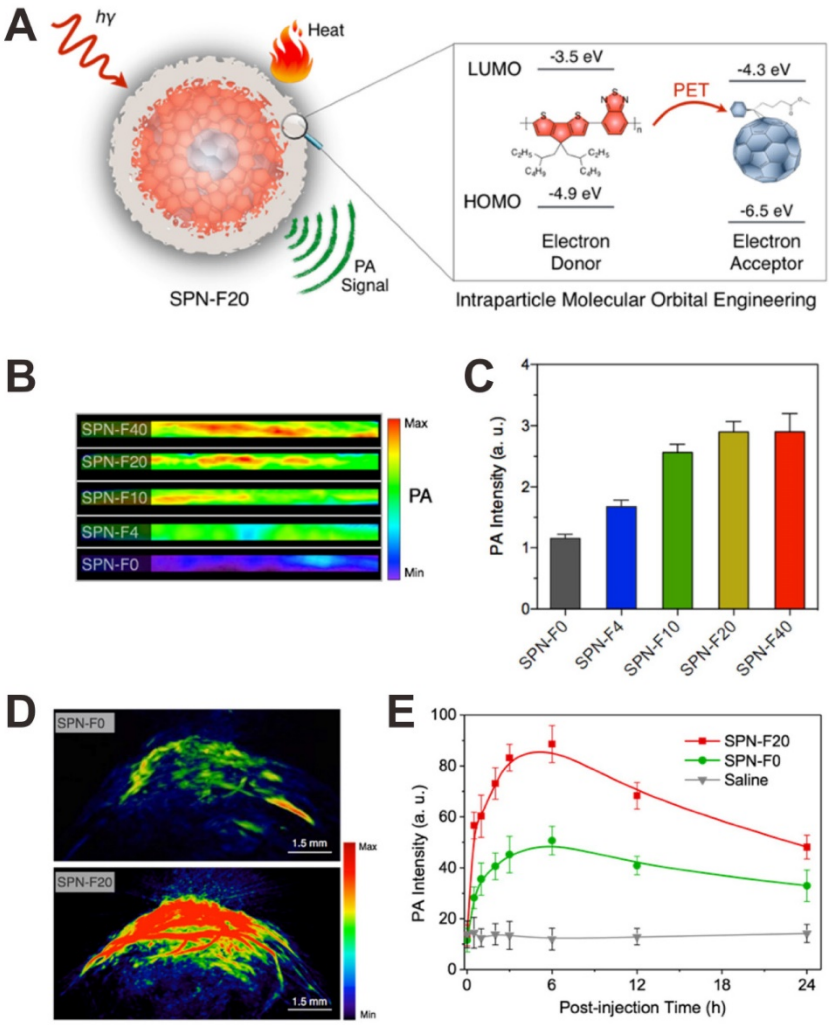

Figure 13. (A) Illustration showing the mechanism of photoinduced electron transfer-induced amplified PA signal. *In vitro* PA images (B) and PA intensities (C) of fullerene doped semiconducting polymer nanoparticle (SPN-F) solutions. (D) PA images of tumor tissues after injection of SPN-F0 and SPN-F20. (E) PA intensities of SPN-F0, SPN-F20, or saline as a function of postinjection time. Reproduced with permission [148]. Copyright 2016 American Chemical Society.

5. Conclusion and outlook

PAI, as a promising real-time imaging technique with high spatial resolution and tissue penetration depth, has been widely studied. This paper briefly summarized recent advances in PAI for biomedical applications, such as deep tumor imaging, therapy monitoring, metabolic imaging, pH detection, enzyme detection, ROS detection, metal ions detection, and so on. To improve PAI sensitivity, various exogenous contrast agents, such as metallic nanomaterials, semimetallic nanomaterials, carbon-based nanomaterials, transition metal chalcogenides, organic dyes, polymer-based nanomaterials, have been developed for PAI in recent years. In order to enhance PA signals, different strategies which are based on synergistic effect of two or more PA contrast agents, plasmonic coupling effect of plasmonic metal nanomaterials, self-assembly of organic dyes, photoinduced electron transfer and background signal deduction have been reported. The exploitation of these strategies not only can improve the PA sensitivity, but also can reduce the dose of PA contrast agents.

Although various PA contrast agents have demonstrated their high PA efficiency and unnoticeable toxicity in pre-clinical studies, they have not been approved for clinical use. In the future, the following directions should be taken into account: 1) Fabrication of activatable PA contrast agents that sense specific stimuli of interest followed by PA signal change in a predictable manner, such as a shift in the absorption peak. By analyzing the differential PA signals, the surrounding PA noises can be reduced and then the selectivity and sensitivity of PAI can be improved. 2) Optimization of targeting PA contrast agents to actively target the tumor, improve the tumor accumulation rate, and reduce the reticuloendothelial system (RES) retention by using specific biomarkers (such as peptides, antibodies, and so on). 3)

Development of new strategies that can further enhance the PA signals of PA contrast agents. The current strategies to amplify the PA signals mainly focus on the improvement of NIR adsorption and photothermal effect by exploiting plasmonic coupling effect, self-assembly or photoinduced electron transfer. 4) Development of PA-based multi-modal contrast agents that can provide complementary information by combining information from various imaging modalities and overcome the weaknesses of each imaging modality. 5) Systematic assessment of the stability, toxicity, biocompability, biodegradability, immunogenicity and pharmacokinetics of PA contrast agents that would be of great help to accelerate their clinical translation for PAI.

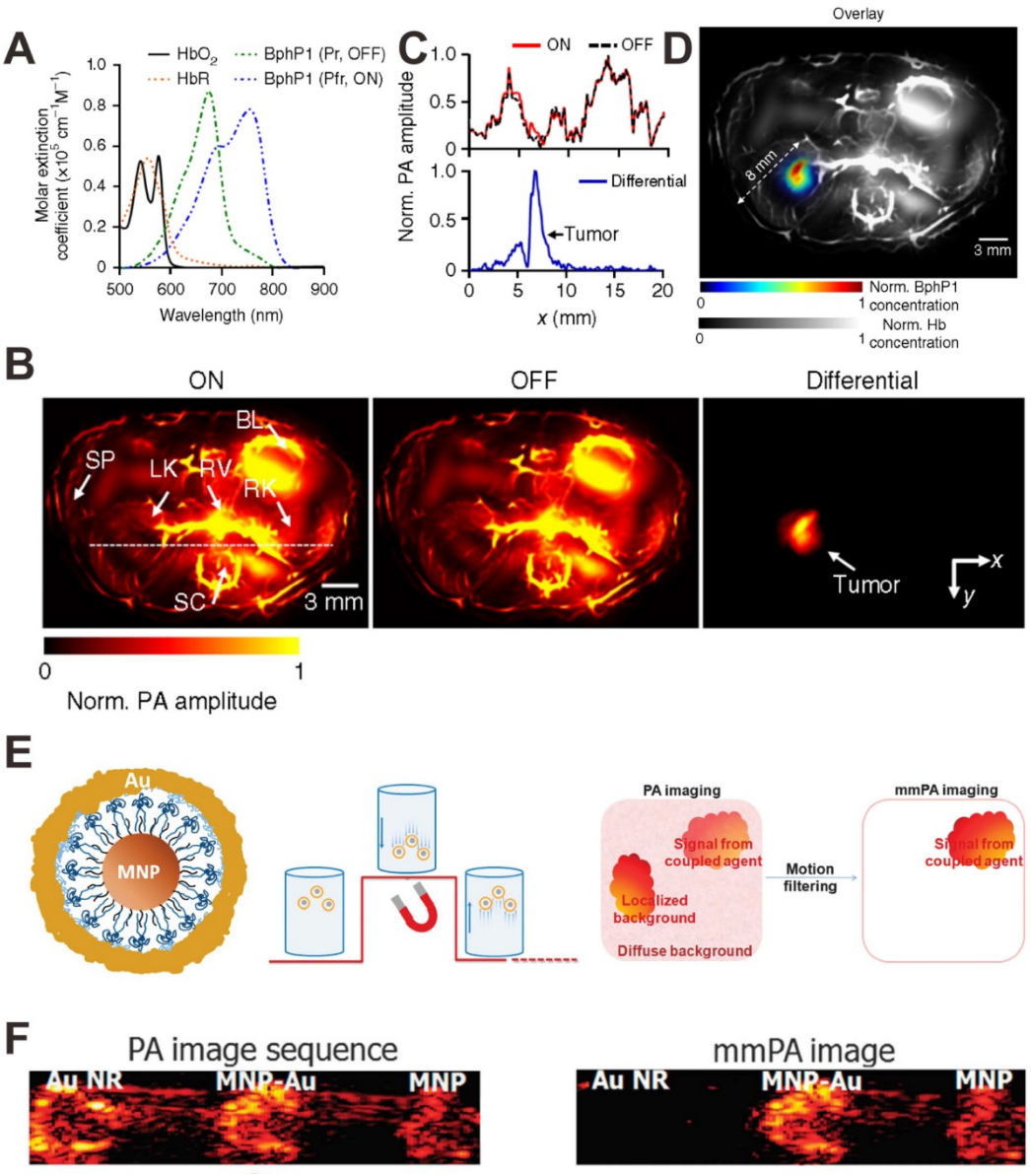

Figure 14. (A) Molar extinction spectra of BphP1 in the ON-state (Pfr) and OFF-state (Pr). (B) *In vivo* PA images of a nude mouse at 1 week after injection of BphP1-expressing tumor cells. (C) Normalized PA signal profiles along the white dashed line in B. (D) An overlay of the tumor (in color) and the blood-dominated OFF-state image (in grayscale). Hb: hemoglobin. Reproduced with permission [149]. Copyright 2016 Nature. (E) Illustration showing the structure of MNP-Au and principle of mmPAI. (F) Conventional PAI and mmPAI of Au NR, MNP-Au and MNP. Reproduced with permission [150]. Copyright 2010 Macmillan Publishers Limited.

Acknowledgment

This work was supported by the National Science Foundation of China (81401465, 51573096), and the Intramural Research Program (IRP) of the NIBIB, NIH.

Competing Interests

The authors have declared that no competing interest exists.

References

1. Jin Y, Gao X. Plasmonic fluorescent quantum dots. Nat Nanotechnol. 2009; 4: 571-6.
2. Wang Y, Zhou K, Huang G, Hensley C, Huang X, Ma X, *et al.* A nanoparticle-based strategy for the imaging of a broad range of tumours by nonlinear amplification of microenvironment signals. Nat Mater. 2014; 13: 204-12.
3. Zrazhevskiy P, Gao X. Multifunctional quantum dots for personalized medicine. Nano Today. 2009; 4: 414-28.
4. Nguyen QT, Tsien RY. Fluorescence-guided surgery with live molecular navigation-a new cutting edge. Nat Rev Cancer. 2013; 13: 653-62.
5. Li Z, Zhang Y, Jiang S. Multicolor core/shell-structured upconversion fluorescent nanoparticles. Adv Mater. 2008; 20: 4765-9.
6. Wang H, Liu Z, Wang S, Dong C, Gong X, Zhao P, *et al.* MC540 and upconverting nanocrystal coloaded polymeric liposome for near-infrared light-triggered photodynamic therapy and cell fluorescent imaging. ACS Appl Mater Interfaces. 2014; 6: 3219-25.
7. Park YI, Kim HM, Kim JH, Moon KC, Yoo B, Lee KT, *et al.* Theranostic probe based on lanthanide-doped nanoparticles for simultaneous *in vivo* dual-modal imaging and photodynamic therapy. Adv Mater. 2012; 24: 5755-61.
8. Yang W, Guo W, Gong X, Zhang B, Wang S, Chen N, *et al.* Facile synthesis of Gd-Cu-In-S/ZnS bimodal quantum dots with optimized properties for tumor targeted fluorescence/MR *in vivo* imaging. ACS Appl Mater Interfaces. 2015; 7: 18759-68.
9. Guo W, Sun X, Jacobson O, Yan X, Min K, Srivatsan A, *et al.* Intrinsically radioactive [^{64}Cu]CuInS/ZnS quantum dots for PET and optical imaging: improved radiochemical stability and controllable Cerenkov luminescence. ACS Nano. 2015; 9: 488-95.
10. Guo W, Chen N, Tu Y, Dong C, Zhang B, Hu C, *et al.* Synthesis of Zn-Cu-In-S/ZnS core/shell quantum dots with inhibited blue-shift photoluminescence and applications for tumor targeted bioimaging. Theranostics. 2013; 3: 99-108.
11. Hong G, Robinson JT, Zhang Y, Diao S, Antaris AL, Wang Q, *et al. In vivo* fluorescence imaging with Ag_2S quantum dots in the second near-infrared region. Angew Chem Int Ed. 2012; 51: 9818-21.
12. Zhang Y, Hong G, Chen G, Li F, Dai H, Wang Q. Ag_2S quantum dot: a bright and biocompatible fluorescent nanoprobe in the second near-infrared window. ACS Nano. 2012; 6: 3695-702.
13. Li C, Li F, Zhang Y, Zhang W, Zhang XE, Wang Q. Real-time monitoring surface chemistry-dependent *in vivo* behaviors of protein nanocages *via* encapsulating an NIR-II Ag_2S quantum dot. ACS Nano. 2015; 9: 12255-63.
14. Wang LV, Hu S. Photoacoustic tomography: *in vivo* imaging from organelles to organs. Science. 2012; 335: 1458-62.
15. Kim C, Favazza C, Wang LV. *In vivo* photoacoustic tomography of chemicals: high-resolution functional and molecular optical imaging at new depths. Chem Rev. 2010; 110: 2756-82.
16. Nie L, Chen X. Structural and functional photoacoustic molecular tomography aided by emerging contrast agents. Chem Soc Rev. 2014; 43: 7132-70.
17. Lin J, Wang S, Huang P, Wang Z, Chen S, Niu G, *et al.* Photosensitizer-loaded gold vesicles with strong plasmonic coupling effect for imaging-guided photothermal/photodynamic therapy. ACS Nano. 2013; 7: 5320-9.
18. Fan Q, Cheng K, Yang Z, Zhang R, Yang M, Hu X, *et al.* Perylene-diimide-based nanoparticles as highly efficient photoacoustic agents for deep brain tumor imaging in living mice. Adv Mater. 2015; 27: 843-7.
19. Hu S, Maslov K, Wang LV. Second-generation optical-resolution photoacoustic microscopy with improved sensitivity and speed. Opt Lett. 2011; 36: 1134-6.
20. Schwarz M, Buehler A, Aguirre J, Ntziachristos V. Three-dimensional multispectral optoacoustic mesoscopy reveals melanin and blood oxygenation in human skin *in vivo*. J Biophotonics. 2016; 9: 55-60.
21. Wang B, Su JL, Amirian J, Litovsky SH, Smalling R, Emelianov S. Detection of lipid in atherosclerotic vessels using ultrasound-guided spectroscopic intravascular photoacoustic imaging. Opt Express. 2010; 18: 4889-97.
22. Favazza CP, Jassim O, Cornelius LA, Wang LV. *In vivo* photoacoustic microscopy of human cutaneous microvasculature and a nevus. J Biomed Opt. 2011; 16: 016015.
23. Ashkenazi S, Huang S-W, Horvath T, Koo Y-EL, Kopelman R. Photoacoustic probing of fluorophore excited state lifetime with application to oxygen sensing. J Biomed Opt. 2008; 13: 034023.
24. Hu S, Wang LV. Optical-resolution photoacoustic microscopy: auscultation of biological systems at the cellular level. Biophys J. 2013; 105: 841-7.
25. Ning B, Kennedy MJ, Dixon AJ, Sun N, Cao R, Soetikno BT, *et al.* Simultaneous photoacoustic microscopy of microvascular anatomy, oxygen saturation, and blood flow. Opt Lett. 2015; 40: 910-3.
26. Laufer J, Johnson P, Zhang E, Treeby B, Cox B, Pedley B, *et al. In vivo* preclinical photoacoustic imaging of tumor vasculature development and therapy. J Biomed Opt. 2012; 17: 056016.
27. Oh J-T, Li M-L, Zhang HF, Maslov K, Stoica G, Wang LV. Three-dimensional imaging of skin melanoma *in vivo* by dual-wavelength photoacoustic microscopy. J Biomed Opt. 2006; 11: 034032.
28. Filonov GS, Krumholz A, Xia J, Yao J, Wang LV, Verkhusha VV. Deep-tissue photoacoustic tomography of a genetically encoded near-infrared fluorescent probe. Angew Chem Int Ed. 2012; 51: 1448-51.
29. Homan KA, Souza M, Truby R, Luke GP, Green C, Vreeland E, *et al.* Silver nanoplate contrast agents for *in vivo* molecular photoacoustic imaging. ACS Nano. 2012; 6: 641-50.
30. Ray A, Mukundan A, Xie Z, Karamchand L, Wang X, Kopelman R. Highly stable polymer coated nano-clustered silver plates: a multimodal optical contrast agent for biomedical imaging. Nanotechnology. 2014; 25: 445104.
31. Nie L, Chen M, Sun X, Rong P, Zheng N, Chen X. Palladium nanosheets as highly stable and effective contrast agents for *in vivo* photoacoustic molecular imaging. Nanoscale. 2014; 6: 1271-6.
32. Chen M, Tang S, Guo Z, Wang X, Mo S, Huang X, *et al.* Core-shell Pd@Au nanoplates as theranostic agents for *in-vivo* photoacoustic imaging, CT imaging, and photothermal therapy. Adv Mater. 2014; 26: 8210-6.
33. Li W, Rong P, Yang K, Huang P, Sun K, Chen X. Semimetal nanomaterials of antimony as highly efficient agent for photoacoustic imaging and photothermal therapy. Biomaterials. 2015; 45: 18-26.
34. Li W, Chen X. Gold nanoparticles for photoacoustic imaging. Nanomedicine. 2015; 10: 299-320.
35. Huang P, Bao L, Zhang C, Lin J, Luo T, Yang D, *et al.* Folic acid-conjugated silica-modified gold nanorods for X-ray/CT imaging-guided dual-mode radiation and photo-thermal therapy. Biomaterials. 2011; 32: 9796-809.
36. Li Z, Huang P, Zhang X, Lin J, Yang S, Liu B, *et al.* RGD-conjugated dendrimer-modified gold nanorods for *in vivo* tumor targeting and photothermal therapy. Mol Pharmaceutics. 2009; 7: 94-104.
37. Chen WH, Yang CX, Qiu WX, Luo GF, Jia HZ, Lei Q, *et al.* Multifunctional theranostic nanoplatform for cancer combined therapy based on gold nanorods. Adv Healthcare Mater. 2015; 4: 2247-59.
38. Zhong J, Wen L, Yang S, Xiang L, Chen Q, Xing D. Imaging-guided high-efficient photoacoustic tumor therapy with targeting gold nanorods. Nanomedicine. 2015; 11: 1499-509.
39. Wang S, Huang P, Nie L, Xing R, Liu D, Wang Z, *et al.* Single continuous wave laser induced photodynamic/plasmonic photothermal therapy using photosensitizer-functionalized gold nanostars. Adv Mater. 2013; 25: 3055-61.
40. Wang S, Teng Z, Huang P, Liu D, Liu Y, Tian Y, *et al.* Reversibly extracellular pH controlled cellular uptake and photothermal therapy by PEGylated mixed-charge gold nanostars. Small. 2015; 11: 1801-10.
41. Zhang YS, Wang Y, Wang L, Cai X, Zhang C, Wang LV, *et al.* Labeling human mesenchymal stem cells with gold nanocages for *in vitro* and *in vivo* tracking by two-photon microscopy and photoacoustic microscopy. Theranostics. 2013; 3: 532-43.
42. Sun T, Wang Y, Wang Y, Xu J, Zhao X, Vangveravong S, *et al.* Using SV119-gold nanocage conjugates to eradicate cancer stem cells through a combination of photothermal and chemo therapies. Adv Healthcare Mater. 2014; 3: 1283-91.
43. Topete A, Alatorre-Meda M, Iglesias P, Villar-Alvarez EM, Barbosa S, Costoya JA, *et al.* Fluorescent drug-loaded, polymeric-based, branched gold nanoshells for localized multimodal therapy and imaging of tumoral cells. ACS Nano. 2014; 8: 2725-38.
44. Song J, Yang X, Jacobson O, Huang P, Sun X, Lin L, *et al.* Ultrasmall gold nanorod vesicles with enhanced tumor accumulation and fast excretion from the body for cancer therapy. Adv Mater. 2015; 27: 4910-7.
45. Huang P, Rong P, Lin J, Li W, Yan X, Zhang MG, *et al.* Triphase interface synthesis of plasmonic gold bellflowers as near-infrared light mediated acoustic and thermal theranostics. J Am Chem Soc. 2014; 136: 8307-13.
46. Huang P, Pandoli O, Wang X, Wang Z, Li Z, Zhang C, *et al.* Chiral guanosine 5'-monophosphate-capped gold nanoflowers: controllable synthesis, characterization, surface-enhanced Raman scattering activity, cellular imaging and photothermal therapy. Nano Research. 2012; 5: 630-9.
47. Zhang L, Rong P, Chen M, Gao S, Zhu L. A novel single walled carbon nanotube (SWCNT) functionalization agent facilitating *in vivo* combined chemo/thermo therapy. Nanoscale. 2015; 7: 16204-13.
48. Huang P, Lin J, Yang D, Zhang C, Li Z, Cui D. Photosensitizer-loaded dendrimer-modified multi-walled carbon nanotubes for photodynamic therapy. J Control Release. 2011; 152: e33-e4.
49. Lin J, Chen X, Huang P. Graphene-based nanomaterials for bioimaging. Adv Drug Delivery Rev. 2016; doi:10.1016/j.addr.2016.05.013.
50. Yan X, Hu H, Lin J, Jin AJ, Niu G, Zhang S, *et al.* Optical and photoacoustic dual-modality imaging guided synergistic photodynamic/photothermal therapies. Nanoscale. 2015; 7: 2520-6.
51. Yan X, Niu G, Lin J, Jin AJ, Hu H, Tang Y, *et al.* Enhanced fluorescence imaging guided photodynamic therapy of sinoporphyrin sodium loaded graphene oxide. Biomaterials. 2015; 42: 94-102.
52. Huang P, Wang S, Wang X, Shen G, Lin J, Wang Z, *et al.* Surface functionalization of chemically reduced graphene oxide for targeted photodynamic therapy. J Biomed Nanotechnol. 2015; 11: 117-25.
53. Huang P, Xu C, Lin J, Wang C, Wang X, Zhang C, *et al.* Folic acid-conjugated graphene oxide loaded with photosensitizers for targeting photodynamic therapy. Theranostics. 2011; 1: 240-50.
54. Lalwani G, Cai X, Nie L, Wang LV, Sitharaman B. Graphene-based contrast agents for photoacoustic and thermoacoustic tomography. Photoacoustics. 2013; 1: 62-7.
55. Sheng Z, Song L, Zheng J, Hu D, He M, Zheng M, *et al.* Protein-assisted fabrication of nano-reduced graphene oxide for combined *in vivo* photoacoustic imaging and photothermal therapy. Biomaterials. 2013; 34: 5236-43.

56. Huang P, Lin J, Wang X, Wang Z, Zhang C, He M, *et al.* Light-triggered theranostics based on photosensitizer-conjugated carbon dots for simultaneous enhanced-fluorescence imaging and photodynamic therapy. Adv Mater. 2012; 24: 5104-10.
57. Ge J, Jia Q, Liu W, Guo L, Liu Q, Lan M, *et al.* Red-emissive carbon dots for fluorescent, photoacoustic, and thermal theranostics in living mice. Adv Mater. 2015; 27: 4169-77.
58. Jiang T, Sun W, Zhu Q, Burns NA, Khan SA, Mo R, *et al.* Furin-mediated sequential delivery of anticancer cytokine and small-molecule drug shuttled by graphene. Adv Mater. 2015; 27: 1021-8.
59. Tian B, Wang C, Zhang S, Feng L, Liu Z. Photothermally enhanced photodynamic therapy delivered by nano-graphene oxide. ACS Nano. 2011; 5: 7000-9.
60. Liu Z, Robinson JT, Sun X, Dai H. PEGylated nanographene oxide for delivery of water-insoluble cancer drugs. J Am Chem Soc. 2008; 130: 10876-7.
61. Rong P, Yang K, Srivastan A, Kiesewetter DO, Yue X, Wang F, *et al.* Photosensitizer loaded nano-graphene for multimodality imaging guided tumor photodynamic therapy. Theranostics. 2014; 4: 229-39.
62. Cheng L, Liu J, Gu X, Gong H, Shi X, Liu T, *et al.* PEGylated WS_2 nanosheets as a multifunctional theranostic agent for *in vivo* dual-modal CT/photoacoustic imaging guided photothermal therapy. Adv Mater. 2014; 26: 1886-93.
63. Yin W, Yan L, Yu J, Tian G, Zhou L, Zheng X, *et al.* High-throughput synthesis of single-layer MoS_2 nanosheets as a near-infrared photothermal-triggered drug delivery for effective cancer therapy. ACS Nano. 2014; 8: 6922-33.
64. Yang K, Yang G, Chen L, Cheng L, Wang L, Ge C, *et al.* FeS nanoplates as a multifunctional nano-theranostic for magnetic resonance imaging guided photothermal therapy. Biomaterials. 2015; 38: 1-9.
65. Cui J, Jiang R, Xu S, Hu G, Wang L. Cu_7S_4 nanosuperlattices with greatly enhanced photothermal efficiency. Small. 2015; 11: 4183-90.
66. Hessel CM, Pattani VP, Rasch M, Panthani MG, Koo B, Tunnell JW, *et al.* Copper selenide nanocrystals for photothermal therapy. Nano Lett. 2011; 11: 2560-6.
67. Li B, Wang Q, Zou R, Liu X, Xu K, Li W, *et al.* $Cu_{7.2}S_4$ nanocrystals: a novel photothermal agent with a 56.7% photothermal conversion efficiency for photothermal therapy of cancer cells. Nanoscale. 2014; 6: 3274-82.
68. Liu J, Zheng X, Yan L, Zhou L, Tian G, Yin W, *et al.* Bismuth sulfide nanorods as a precision nanomedicine for *in vivo* multimodal imaging-guided photothermal therapy of tumor. ACS Nano. 2015; 9: 696-707.
69. Song X, Wang X, Yu S, Cao J, Li S, Li J, *et al.* Co_9Se_8 nanoplates as a new theranostic platform for photoacoustic/magnetic resonance dual-modal-imaging-guided chemo-photothermal combination therapy. Adv Mater. 2015; 27: 3285-91.
70. Zhang L, Gao S, Zhang F, Yang K, Ma Q, Zhu L. Activatable hyaluronic acid nanoparticle as a theranostic agent for optical/photoacoustic image-guided photothermal therapy. ACS Nano. 2014; 8: 12250-8.
71. Gao D, Zhang P, Liu C, Chen C, Gao G, Wu Y, *et al.* Compact chelator-free Ni-integrated CuS nanoparticles with tunable near-infrared absorption and enhanced relaxivity for *in vivo* dual-modal photoacoustic/MR imaging. Nanoscale. 2015; 7: 17631-6.
72. Zhou M, Ku G, Pageon L, Li C. Theranostic probe for simultaneous *in vivo* photoacoustic imaging and confined photothermolysis by pulsed laser at 1064 nm in 4T1 breast cancer model. Nanoscale. 2014; 6: 15228-35.
73. Wang Z, Huang P, Jacobson O, Liu Y, Lin L, Lin J, *et al.* Biomineralization-inspired synthesis of copper sulfide-ferritin nanocages as cancer theranostics. ACS Nano. 2016; 10: 3453-60.
74. Lewinski N, Colvin V, Drezek R. Cytotoxicity of nanoparticles. Small. 2008; 4: 26-49.
75. Sun C, Wen L, Zeng J, Wang Y, Sun Q, Deng L, *et al.* One-pot solventless preparation of PEGylated black phosphorus nanoparticles for photoacoustic imaging and photothermal therapy of cancer. Biomaterials. 2016; 91: 81-9.
76. Wang H, Yang X, Shao W, Chen S, Xie J, Zhang X, *et al.* Ultrathin black phosphorus nanosheets for efficient singlet oxygen generation. J Am Chem Soc. 2015; 137: 11376-82.
77. Sheng Z, Hu D, Zheng M, Zhao P, Liu H, Gao D, *et al.* Smart human serum albumin-indocyanine green nanoparticles generated by programmed assembly for dual-modal imaging-guided cancer synergistic phototherapy. ACS Nano. 2014; 8: 12310-22.
78. Wang Y, Yang T, Ke H, Zhu A, Wang Y, Wang J, *et al.* Smart albumin-biomineralized nanocomposites for multimodal imaging and photothermal tumor ablation. Adv Mater. 2015; 27: 3874-82.
79. Lovell JF, Jin CS, Huynh E, Jin H, Kim C, Rubinstein JL, *et al.* Porphysome nanovesicles generated by porphyrin bilayers for use as multimodal biophotonic contrast agents. Nat Mater. 2011; 10: 324-32.
80. Shan G, Weissleder R, Hilderbrand SA. Upconverting organic dye doped core-shell nano-composites for dual-modality NIR imaging and photo-thermal therapy. Theranostics. 2013; 3: 267-74.
81. Tan X, Luo S, Wang D, Su Y, Cheng T, Shi C. A NIR heptamethine dye with intrinsic cancer targeting, imaging and photosensitizing properties. Biomaterials. 2012; 33: 2230-9.
82. Lim C-K, Shin J, Lee Y-D, Kim J, Oh KS, Yuk SH, *et al.* Phthalocyanine-aggregated polymeric nanoparticles as tumor-homing near-infrared absorbers for photothermal therapy of cancer. Theranostics. 2012; 2: 871-9.
83. Song X, Chen Q, Liu Z. Recent advances in the development of organic photothermal nano-agents. Nano Research. 2015; 8: 340-54.
84. Rong P, Huang P, Liu Z, Lin J, Jin A, Ma Y, *et al.* Protein-based photothermal theranostics for imaging-guided cancer therapy. Nanoscale. 2015; 7: 16330-6.
85. Chen Q, Liang C, Wang C, Liu Z. An imagable and photothermal "abraxane-like" nanodrug for combination cancer therapy to treat subcutaneous and metastatic breast tumors. Adv Mater. 2015; 27: 903-10.
86. Huang P, Rong P, Jin A, Yan X, Zhang MG, Lin J, *et al.* Dye-loaded ferritin nanocages for multimodal imaging and photothermal therapy. Adv Mater. 2014; 26: 6401-8.
87. Yang J, Choi J, Bang D, Kim E, Lim E-K, Park H, *et al.* Convertible organic nanoparticles for near-infrared photothermal ablation of cancer cells. Angew Chem Int Ed. 2011; 50: 441-4.
88. Lin L-S, Cong Z-X, Cao J-B, Ke K-M, Peng Q-L, Gao J, *et al.* Multifunctional Fe_3O_4@ polydopamine core-shell nanocomposites for intracellular mRNA detection and imaging-guided photothermal therapy. ACS Nano. 2014; 8: 3876-83.
89. Yang K, Xu H, Cheng L, Sun C, Wang J, Liu Z. *In vitro* and *in vivo* near-infrared photothermal therapy of cancer using polypyrrole organic nanoparticles. Adv Mater. 2012; 24: 5586-92.
90. Pu K, Mei J, Jokerst JV, Hong G, Antaris AL, Chattopadhyay N, *et al.* Diketopyrrolopyrrole-based semiconducting polymer nanoparticles for *in vivo* photoacoustic imaging. Adv Mater. 2015; 27: 5184-90.
91. Lin J, Wang M, Hu H, Yang X, Wen B, Wang Z, *et al.* Multimodal-imaging-guided cancer phototherapy by versatile biomimetic theranostics with UV and gamma-irradiation protection. Adv Mater. 2016; 28: 3273-9.
92. Song X, Liang C, Gong H, Chen Q, Wang C, Liu Z. Photosensitizer-conjugated albumin-polypyrrole nanoparticles for imaging-guided *in vivo* photodynamic/photothermal therapy. Small. 2015; 11: 3932-41.
93. Tian Q, Wang Q, Yao KX, Teng B, Zhang J, Yang S, *et al.* Multifunctional polypyrrole@ Fe_3O_4 nanoparticles for dual-modal imaging and *in vivo* photothermal cancer therapy. Small. 2014; 10: 1063-8.
94. Liang X, Li Y, Li X, Jing L, Deng Z, Yue X, *et al.* PEGylated polypyrrole nanoparticles conjugating gadolinium chelates for dual-modal MRI/photoacoustic imaging guided photothermal therapy of cancer. Adv Funct Mater. 2015; 25: 1451-62.
95. Wang C, Xu H, Liang C, Liu Y, Li Z, Yang G, *et al.* Iron oxide@ polypyrrole nanoparticles as a multifunctional drug carrier for remotely controlled cancer therapy with synergistic antitumor effect. ACS Nano. 2013; 7: 6782-95.
96. Jin Y, Li Y, Ma X, Zha Z, Shi L, Tian J, *et al.* Encapsulating tantalum oxide into polypyrrole nanoparticles for X-ray CT/photoacoustic bimodal imaging-guided photothermal ablation of cancer. Biomaterials. 2014; 35: 5795-804.
97. Zhang R, Fan Q, Yang M, Cheng K, Lu X, Zhang L, *et al.* Engineering melanin nanoparticles as an efficient drug-delivery system for imaging-guided chemotherapy. Adv Mater. 2015; 27: 5063-9.
98. Chen M, Fang X, Tang S, Zheng N. Polypyrrole nanoparticles for high-performance *in vivo* near-infrared photothermal cancer therapy. Chem Commun. 2012; 48: 8934-6.
99. Cheng L, Yang K, Chen Q, Liu Z. Organic stealth nanoparticles for highly effective *in vivo* near-infrared photothermal therapy of cancer. ACS Nano. 2012; 6: 5605-13.
100. Zhou Y, Wang D, Zhang Y, Chitgupi U, Geng J, Wang Y, *et al.* A phosphorus phthalocyanine formulation with intense absorbance at 1000 nm for deep optical imaging. Theranostics. 2016; 6: 688-97.
101. Cheng Z, Al Zaki A, Hui JZ, Muzykantov VR, Tsourkas A. Multifunctional nanoparticles: cost versus benefit of adding targeting and imaging capabilities. Science. 2012; 338: 903-10.
102. Peer D, Karp JM, Hong S, Farokhzad OC, Margalit R, Langer R. Nanocarriers as an emerging platform for cancer therapy. Nat Nanotechnol. 2007; 2: 751-60.
103. Nie L, Huang P, Li W, Yan X, Jin A, Wang Z, *et al.* Early-stage imaging of nanocarrier-enhanced chemotherapy response in living subjects by scalable photoacoustic microscopy. ACS Nano. 2014; 8: 12141-50.
104. Mallidi S, Watanabe K, Timerman D, Schoenfeld D, Hasan T. Prediction of tumor recurrence and therapy monitoring using ultrasound-guided photoacoustic imaging. Theranostics. 2015; 5: 289-301.
105. Bohndiek SE, Sasportas LS, Machtaler S, Jokerst JV, Hori S, Gambhir SS. Photoacoustic tomography detects early vessel regression and normalization during ovarian tumor response to the antiangiogenic therapy trebananib. J Nucl Med. 2015; 56: 1942-7.
106. Rich LJ, Seshadri M. Photoacoustic monitoring of tumor and normal tissue response to radiation. Sci Rep. 2016; 6: 21237.
107. Zhao T, Shen X, Li L, Guan Z, Gao N, Yuan P, *et al.* Gold nanorods as dual photo-sensitizing and imaging agents for two-photon photodynamic therapy. Nanoscale. 2012; 4: 7712-9.
108. Chen B, Pogue BW, Hoopes PJ, Hasan T. Combining vascular and cellular targeting regimens enhances the efficacy of photodynamic therapy. Int J Radiat Oncol Biol Phys. 2005; 61: 1216-26.
109. Chatni MR, Xia J, Sohn R, Maslov K, Guo Z, Zhang Y, *et al.* Tumor glucose metabolism imaged *in vivo* in small animals with whole-body photoacoustic computed tomography. J Biomed Opt. 2012; 17: 076012.
110. Webb BA, Chimenti M, Jacobson MP, Barber DL. Dysregulated pH: a perfect storm for cancer progression. Nat Rev Cancer. 2011; 11: 671-7.
111. Cuajungco MP, Faget KY. Zinc takes the center stage: its paradoxical role in Alzheimer's disease. Brain Res Rev. 2003; 41: 44-56.

112. Coakley RJ, Taggart C, McElvaney NG, O'Neill SJ. Cytosolic pH and the inflammatory microenvironment modulate cell death in human neutrophils after phagocytosis. Blood. 2002; 100: 3383-91.
113. Bandmann O, Weiss KH, Kaler SG. Wilson's disease and other neurological copper disorders. Lancet Neurol. 2015; 14: 103-13.
114. Lippert AR, De Bittner GCV, Chang CJ. Boronate oxidation as a bioorthogonal reaction approach for studying the chemistry of hydrogen peroxide in living systems. Acc Chem Res. 2011; 44: 793-804.
115. Li D, Shi Y, Tian X, Wang M, Huang B, Li F, *et al.* Fluorescent probes with dual-mode for rapid detection of SO_2 derivatives in living cells: ratiometric and two-photon fluorescent sensors. Sens Actuators B. 2016; 233: 1-6.
116. Jin Q, Feng L, Wang D-D, Wu J-J, Hou J, Dai Z-R, *et al.* A highly selective near-infrared fluorescent probe for carboxylesterase 2 and its bioimaging applications in living cells and animals. Biosens Bioelectron. 2016; 83: 193-9.
117. Zheng Z, Wang L, Tang W, Chen P, Zhu H, Yuan Y, *et al.* Hydrazide D-luciferin for *in vitro* selective detection and intratumoral imaging of Cu^{2+}. Biosens Bioelectron. 2016; 83: 200-4.
118. Liu K, Shang H, Kong X, Ren M, Wang J-Y, Liu Y, *et al.* A novel near-infrared fluorescent probe for H_2O_2 in alkaline environment and the application for H_2O_2 imaging *in vitro* and *in vivo*. Biomaterials. 2016; 100: 162-71.
119. Chen Q, Liu X, Chen J, Zeng J, Cheng Z, Liu Z. A self-assembled albumin-based nanoprobe for *in vivo* ratiometric photoacoustic pH imaging. Adv Mater. 2015; 27: 6820-7.
120. Chen Q, Liu X, Zeng J, Cheng Z, Liu Z. Albumin-NIR dye self-assembled nanoparticles for photoacoustic pH imaging and pH-responsive photothermal therapy effective for large tumors. Biomaterials. 2016; 98: 23-30.
121. Guha S, Shaw GK, Mitcham TM, Bouchard RR, Smith BD. Croconaine rotaxane for acid activated photothermal heating and ratiometric photoacoustic imaging of acidic pH. Chem Commun. 2016; 52: 120-3.
122. Miao Q, Lyu Y, Ding D, Pu K. Semiconducting oligomer nanoparticles as an activatable photoacoustic probe with amplified brightness for *in vivo* imaging of pH. Adv Mater. 2016; 28: 3662-8.
123. Qin H, Zhao Y, Zhang J, Pan X, Yang S, Xing D. Inflammation-targeted gold nanorods for intravascular photoacoustic imaging detection of matrix metalloproteinase-2 (MMP 2) in atherosclerotic plaques. Nanomed Nanotechnol. 2016; 12: 1765-74.
124. Yang K, Zhu L, Nie L, Sun X, Cheng L, Wu C, *et al.* Visualization of protease activity *in vivo* using an activatable photo-acoustic imaging probe based on CuS nanoparticles. Theranostics. 2014; 4: 134-41.
125. Pu K, Shuhendler AJ, Jokerst JV, Mei J, Gambhir SS, Bao Z, *et al.* Semiconducting polymer nanoparticles as photoacoustic molecular imaging probes in living mice. Nat Nanotechnol. 2014; 9: 233-9.
126. Li H, Zhang P, Smaga LP, Hoffman RA, Chan J. Photoacoustic probes for ratiometric imaging of copper(II). J Am Chem Soc. 2015; 137: 15628-31.
127. Kessenbrock K, Plaks V, Werb Z. Matrix metalloproteinases: regulators of the tumor microenvironment. Cell. 2010; 141: 52-67.
128. Shuhendler AJ, Pu K, Cui L, Uetrecht JP, Rao J. Real-time imaging of oxidative and nitrosative stress in the liver of live animals for drug-toxicity testing. Nat Biotechnol. 2014; 32: 373-80.
129. Cash KJ, Li C, Xia J, Wang LV, Clark HA. Optical drug monitoring: photoacoustic imaging of nanosensors to monitor therapeutic lithium *in vivo*. ACS nano. 2015; 9: 1692-8.
130. Liu Y, Su Q, Chen M, Dong Y, Shi Y, Feng W, *et al.* Near-infrared upconversion chemodosimeter for *in vivo* detection of Cu^{2+} in wilson disease. Adv Mater. 2016; doi: 10.1002/adma.201601140.
131. Li X, Wu Y, Liu Y, Zou X, Yao L, Li F, *et al.* Cyclometallated ruthenium complex-modified upconversion nanophosphors for selective detection of Hg^{2+} ions in water. Nanoscale. 2014; 6: 1020-8.
132. Liu Y, Chen M, Cao T, Sun Y, Li C, Liu Q, *et al.* A cyanine-modified nanosystem for *in vivo* upconversion luminescence bioimaging of methylmercury. J Am Chem Soc. 2013; 135: 9869-76.
133. Wang Y-W, Fu Y-Y, Peng Q, Guo S-S, Liu G, Li J, *et al.* Dye-enhanced graphene oxide for photothermal therapy and photoacoustic imaging. J Mater Chem B. 2013; 1: 5762-7.
134. Lin LS, Yang X, Niu G, Song J, Yang HH, Chen X. Dual-enhanced photothermal conversion properties of reduced graphene oxide-coated gold superparticles for light-triggered acoustic and thermal theranostics. Nanoscale. 2016; 8: 2116-22.
135. Moon H, Kumar D, Kim H, Sim C, Chang J-H, Kim J-M, *et al.* Amplified photoacoustic performance and enhanced photothermal stability of reduced graphene oxide coated gold nanorods for sensitive photoacoustic imaging. ACS Nano. 2015; 9: 2711-9.
136. de la Zerda A, Liu Z, Bodapati S, Teed R, Vaithilingam S, Khuri-Yakub BT, *et al.* Ultrahigh sensitivity carbon nanotube agents for photoacoustic molecular imaging in living mice. Nano Lett. 2010; 10: 2168-72.
137. Song J, Yang X, Jacobson O, Lin L, Huang P, Niu G, *et al.* Sequential drug release and enhanced photothermal and photoacoustic effect of hybrid reduced graphene oxide-loaded ultrasmall gold nanorod vesicles for cancer therapy. ACS Nano. 2015; 9: 9199-209.
138. de la Zerda A, Bodapati S, Teed R, May SY, Tabakman SM, Liu Z, *et al.* Family of enhanced photoacoustic imaging agents for high-sensitivity and multiplexing studies in living mice. ACS Nano. 2012; 6: 4694-701.
139. Zhang P, Guo Y. Surface-enhanced Raman scattering inside metal nanoshells. J Am Chem Soc. 2009; 131: 3808-9.
140. Liu N, Giessen H. Coupling effects in optical metamaterials. Angew Chem Int Ed. 2010; 49: 9838-52.
141. Huang P, Lin J, Li W, Rong P, Wang Z, Wang S, *et al.* Biodegradable gold nanovesicles with an ultrastrong plasmonic coupling effect for photoacoustic imaging and photothermal therapy. Angew Chem Int Ed. 2013; 52: 13958-64.
142. Liu Y, He J, Yang K, Yi C, Liu Y, Nie L, *et al.* Folding up of gold nanoparticle strings into plasmonic vesicles for enhanced photoacoustic imaging. Angew Chem Int Ed. 2015; 127: 16035-8.
143. Wurthner F, Kaiser TE, Saha-Moller CR. *J*-aggregates: from serendipitous discovery to supramolecular engineering of functional dye materials. Angew Chem Int Ed. 2011; 50: 3376-410.
144. Zhang D, Qi GB, Zhao YX, Qiao SL, Yang C, Wang H. In situ formation of nanofibers from purpurin18-peptide conjugates and the assembly induced retention effect in tumor sites. Adv Mater. 2015; 27: 6125-30.
145. Li LL, Ma HL, Qi GB, Zhang D, Yu F, Hu Z, *et al.* Pathological-condition-driven construction of supramolecular nanoassemblies for bacterial infection detection. Adv Mater. 2016; 28: 254-62.
146. Shakiba M, Ng KK, Huynh E, Chan H, Charron DM, Chen J, *et al.* Stable *J*-aggregation enabled dual photoacoustic and fluorescence nanoparticles for intraoperative cancer imaging. Nanoscale. 2016; 8: 12618-25.
147. Huang P, Gao Y, Lin J, Hu H, Liao H-S, Yan X, *et al.* Tumor-specific formation of enzyme-instructed supramolecular self-assemblies as cancer theranostics. ACS Nano. 2015; 9: 9517-27.
148. Lyu Y, Fang Y, Miao Q, Zhen X, Ding D, Pu K. Intraparticle molecular orbital engineering of semiconducting polymer nanoparticles as amplified theranostics for *in vivo* photoacoustic imaging and photothermal therapy. ACS Nano. 2016; 10: 4472-81.
149. Yao J, Kaberniuk AA, Li L, Shcherbakova DM, Zhang R, Wang L, *et al.* Multiscale photoacoustic tomography using reversibly switchable bacterial phytochrome as a near-infrared photochromic probe. Nat Methods. 2016; 13: 67-73.
150. Jin Y, Jia C, Huang S-W, O'Donnell M, Gao X. Multifunctional nanoparticles as coupled contrast agents. Nat Commun. 2010; 1: 41.